Supplementary Information

Optimized Carrier Extraction at Interfaces for 23.6% Efficient Tin–Lead Perovskite Solar Cells

Shuaifeng Hu,[a] Kento Otsuka,[a] Richard Murdey,[a] Tomoya Nakamura,[a] Minh Anh Truong,[a] Takumi Yamada,[a] Taketo Handa,[a] Kazuhiro Matsuda,[b] Kyohei Nakano,[c] Atsushi Sato,[d] Kazuhiro Marumoto,[d] Keisuke Tajima,[c] Yoshihiko Kanemitsu,[a] Atsushi Wakamiya*[,a]

[a]*Institute for Chemical Research, Kyoto University, Gokasho, Uji, Kyoto 611-0011, Japan.*

[b]*Surface Science Laboratories, Toray Research Center, Inc., 3-3-7, Sonoyama, Otsu, Shiga 520-8567, Japan.*

[c]*RIKEN Center for Emergent Matter Science (CEMS), Wako, Saitama 351-0198, Japan.*

[d]*Division of Materials Science, University of Tsukuba, Tsukuba, Ibaraki 305-8573, Japan.*

*Corresponding author. E-mail: wakamiya@scl.kyoto-u.ac.jp

This Supplementary Information includes:

- Experimental Section
- Supplementary Figures 1 to 40
- Supplementary Tables 1 to 7
- Supplementary References (1–9)

Experimental Section

Materials

Unless otherwise stated, all materials were used as received without further purification. Methylammonium iodide (MAI, > 99.0%), formamidinium iodide (FAI, > 98.0%), bathocuproine (BCP), lead(II) iodide (PbI_2, 99.99%, trace metals basis), and cesium iodide (CsI, > 99%) were purchased from Tokyo Chemical Industry Co., Ltd. (TCI). Ammonium thiocyanate (NH_4SCN, 99.99% trace metals basis), tin(II) fluoride (SnF_2, 99%), and tin(II) iodide (SnI_2, beads, 99.99%, trace metals basis), ethane-1,2-diammonium iodide (ethylenediammonium diiodide, $EDAI_2$, ≥ 98%), glycine hydrochloride (GlyHCl, ≥ 99%), poly[bis(4-phenyl)(2,4,6-trimethylphenyl)amine] (PTAA), and poly(methyl methacrylate) (PMMA) were purchased from Sigma-Aldrich Co., Ltd. (Sigma-Aldrich). Poly(3,4-ethylenedioxythiophene): poly(styrene sulfonate) (PEDOT:PSS) aqueous solution (Clevious PVP AI 4083) was purchased from Heraeus Co., Ltd. Fullerene C_{60} (sublimed, 99.99%) was purchased from ATR Company. 2,3,5,6-Tetrafluoro-7,7,8,8-tetracyanoquinodimethane (F4-TCNQ) was purchased from Ossila. Dehydrated dimethylsulfoxide (DMSO, super dehydrated) and isopropanol (IPA, super dehydrated) were purchased from FUJIFILM Wako Pure Chemical Co., Ltd. Dimethylformamide (DMF), toluene and chlorobenzene were purchased from Kanto Chemical. Co., Inc. All of these solvents were degassed by Ar gas bubbling for 1 h and further dried over molecular sieves (3 Å) in an Ar-filled glove box (H_2O, O_2 < 0.1 ppm) before use.

Fabrication of Perovskite Thin Films

The perovskite film preparation was conducted in an Ar-filled glove box (H_2O, O_2 < 0.1 ppm). The $Cs_{0.1}FA_{0.6}MA_{0.3}Sn_{0.5}Pb_{0.5}I_3$ perovskite precursor solution was prepared by mixing CsI (46.8 mg, 0.180 mmol), FAI (185.7 mg, 1.08 mmol), MAI (85.8 mg, 0.540 mmol), SnI_2 (335.3 mg, 0.900 mmol), PbI_2 (414.9 mg, 0.900 mmol), SnF_2 (14.1 mg, 0.090 mmol), and

NH_4SCN (2.7 mg, 0.036 mmol) in mixed solvents of 0.25 mL DMSO and 0.75 mL DMF to reach a concentration of 1.8 M. To prepare the samples with glycine additive, 2 mol% (4.0 mg, 0.036 mmol) of GlyHCl with respect to the total amount of SnI_2 and PbI_2 was added to the precursor solution. The precursor solution was stirred at 45 °C for 40 min and filtered through a 0.20 μm PTFE filter before use. To spin coat the precursor films, 200 μL of the room temperature precursor solution was applied to the substrate. A two-step spin coating program was used. The first step was at 1000 rpm for 10 s with an acceleration of 200 rpm s^{-1}, and the second step was 4000 rpm for 40 s with an acceleration of 1000 rpm s^{-1}. Room temperature chlorobenzene (400 μL) was used as the antisolvent. The chlorobenzene was quickly dripped onto the surface of the spinning substrate over an interval of 1 s during the second spin coating step at 20 s before the end of the procedure. The substrate was then immediately annealed on a 100 °C hot plate for 10 min, followed by annealing at 65 °C for over 10 min. For the $EDAI_2$ post-treatment, 1.0 mg $EDAI_2$ was added to 1.0 mL IPA and 1.0 mL toluene. The mixed solvent solution was stirred at 70 °C for 3 h and then filtered through a 0.20 μm PTFE filter before spin coating. 120 μL of the $EDAI_2$ solution was applied to the annealed and cooled perovskite films by spin coating at 4000 rpm for 20 s with an acceleration of 1333 rpm s^{-1}. Following spin coating, the films were immediately annealed again at 100 °C for around 5 min.

The composition of the co-solvent system (isopropanol and toluene with the volume ratio of 1:1) used for the $EDAI_2$ post treatment is extremely important. The polarity of the isopropanol helps the organic ammonium salts to anchor to the film surface, enhancing defect passivation[1]. Sn-containing perovskites are soluble in isopropanol[2], however, so we add toluene to reduce the overall viscosity of the solution to accelerate the dispersion of the $EDAI_2$ solution before the spinning.

For the space-charge-limited current (SCLC) measurements, hole-only and electron-only devices were prepared. For the hole-only devices, 150 μL PTAA solution (20 mg mL^{-1} in chlorobenzene, doped with 1 wt% F4-TCNQ), was spin-coated onto the perovskite films fabricated on the PEDOT:PSS-coated substrates at 2000 rpm for 30 s with an acceleration of

400 rpm s^{-1}, and the films were immediately annealed at 65 °C for around 5 min. For the electron-only devices, double-sided C_{60} layers (20 nm) were sequentially deposited by thermal evaporation before and after the perovskite layer preparation. For all samples, 100 nm of silver was deposited through a metallic aperture mask to form the top electrode.

Fabrication of solar cell devices

Glass/FTO substrates (10 Ω sq^{-1}, AGC Inc.) were etched with zinc powder and HCl (6 M in de-ionized water), and consecutively cleaned with 15 min ultrasonic bath in water, acetone, detergent solution (Semico Clean 56, Furuuchi chemical), water, and isopropanol, followed by drying with an air gun, and finally plasma treatment. The PEDOT:PSS hole transport layer was fabricated from an aqueous dispersion which was filtered through a 0.45 μm PVDF filter and then spin coated on the FTO substrate using a spin program of 10 s at 500 rpm followed by 30 s at 4000 rpm. The films were then annealed in air at 140 °C for 20 min. After transferring to an Ar-filled glove box (H_2O, O_2 < 0.1 ppm), the substrates were degassed at 140 °C for 30 min. The perovskite layer was fabricated on PEDOT:PSS following the above-mentioned procedure. The samples were moved under Ar to a vacuum deposition chamber, where 20 nm of C_{60} (deposition rate 0.01 nm s^{-1}) and 8 nm of BCP (deposition rate 0.01 nm s^{-1}) were deposited by thermal evaporation. The top electrode was prepared by depositing 100 nm of silver (deposition rate 0.005 nm s^{-1}) through a shadow mask.

Characterization

For the time-resolved photoluminescence (TRPL) measurements, the samples were excited by a picosecond pulsed laser with a wavelength of 688 nm (Advanced Laser Diode System) and the excitation frequency of 10 kHz. To shorten the measurement time, the PL signal was divided with a beam splitter (transmission 50%) and detected with a pair of avalanche photodiodes (APD) (ID Quantique). The TRPL signal on each APD was recorded using time-correlated single photon counting boards (PicoQuant). Under weak excitation conditions, a

defocus lens was used in order to maintain a high incident photon flux into the APDs. The initial carrier densities were calculated from the excitation photon flux and the absorption coefficient of samples at 688 nm (4.4×10^4 cm^{-1}, Fig. S20). Using a variable neutral density filter, the excitation laser power was adjusted to achieve the desired initial carrier density. The TRPL dynamics were analyzed by the rate equation model reported in our previous work[3].

Scanning electron microscopy (SEM) was performed with a Hitachi S8010 ultra-high-resolution scanning electron microscope (Hitachi High-Tech Corporation).

UV–vis absorption measurement was performed with a Shimadzu UV-3600 plus spectrometer (Shimadzu Co.,).

X-ray photoelectron spectroscopy (XPS) was recorded with a JPS-9010 (JEOL Co., Ltd.) instrument. Perovskite film samples for XPS measurements were prepared in an Ar-filled glove box and transferred to the XPS chamber through an Ar-filled transfer vessel in order to avoid oxygen contamination.

Photocurrent–voltage (*J–V*) curves were measured in a N_2-filled glove box (H_2O, O_2 < 0.1 ppm) with an OTENTO-SUN-P1G solar simulator (Bunkoukeiki Co., Ltd.) and a Keithley 2400 source meter. The light intensity of the illumination source was calibrated using a standard BS520 silicon photodiode. The device active area was defined by an optimal mask, 0.0985 cm^2 for the regular devices and 1.00 cm^2 for the large area cells.

External quantum efficiency (EQE) and internal quantum efficiency (IQE) spectra were measured with a Bunkoukeiki SMO-250III system equipped with a Bunkoukeiki SM-250 diffuse reflection unit (Bunkoukeiki Co., Ltd.). The incident light intensity was calibrated with a standard SiPD S1337-1010BQ silicon photodiode.

UPS was performed with a photoelectron spectroscopy system (PHI5000 Versa Probe II, ULVAC-PHI Inc.) with He I excitation (21.22 eV). A −5.0 V bias was applied to the samples. The chamber base pressure was approximately 1×10^{-6} Pa. Samples were transferred from the glove box to the UPS chamber without exposure to air.

ESR measurements were performed with an X-band ESR spectrometer (JEOL RESONANCE, JES-FA200). The parameters for the measurement are as follow. Sweep range, 319±5 mT; sweep time, 2 min; microwave power, 0.5 mW; modulation frequency, 100 kHz; modulation width, 0.3 mT; time constant, 0.1 s; amplitude, 4000; number of scans (accumulation), 29×10.

Quantum yields were determined with a Hamamatsu Photonics Quantaurus-QY Plus C13534 with calibrated integrating sphere system.

Electrochemical impedance spectroscopy data were obtained in inert atmosphere under AM 1.5G simulated solar radiation, using an Agilent E4990A impedance analyzer. Scans were taken from 20 Hz to 20 MHz, with a 30 mV oscillator voltage, recorded for forward bias voltages between 0 and 1.2 V in 0.1 V steps.

Time-of-flight secondary ion mass spectrometry (ToF-SIMS) measurements were carried out using a ToF.SIMS 5 (IONTOF GmbH) operated in the high lateral resolution mode (burst alignment mode). A 50 kV Bi_3^{2+} primary ion beam with pulses width of 125 ns was used for data acquisition. Primary ion dose density (PIDD) was maintained less than approximately 5×10^{11} ions cm^{-2} in each measurement cycles to prevent sample damage from the irradiation of primary ion beam. For sample etching, a 10 kV Ar gas cluster ion beam (Ar-GCIB) with a center size of approximately 1200 atoms was used as sputtering ion beam. The raster area of the primary ion beam was 30 μm×30 μm and that of the sputtering ion beam was 500×500. Depth profiles and three-dimensional images of $EDAI_2$/GlyHCl-treated ingredients (or ions) were reconstructed from the raw data after data acquisition. In addition, mass spectra and depth profiles with high mass resolution were acquired from an area of 200 μm×200 μm by using high mass resolution mode (bunching mode). A low-energy electron-flood gun was used for charge compensation.

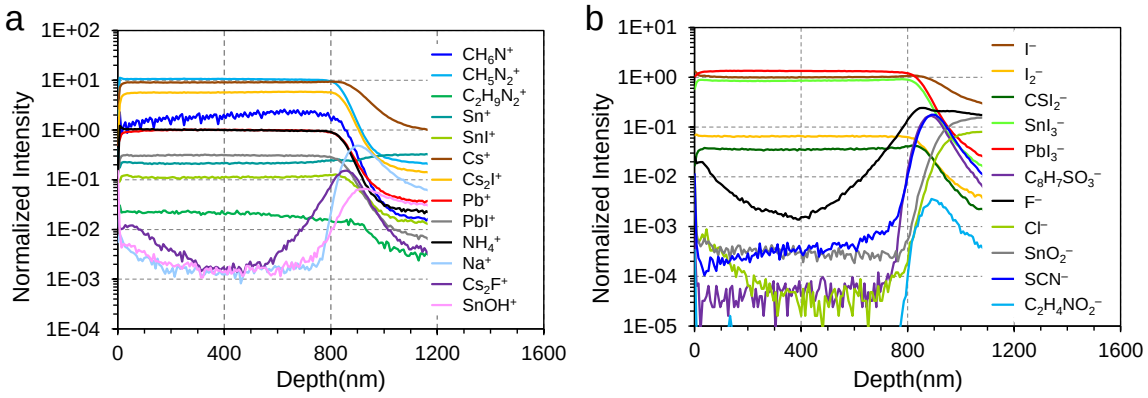

Fig. S1. ToF-SIMS depth profiles of the control perovskite film fabricated on an PEDOT:PSS/FTO-coated glass substrate, measured in **a,** positive and **b,** negative polarity.

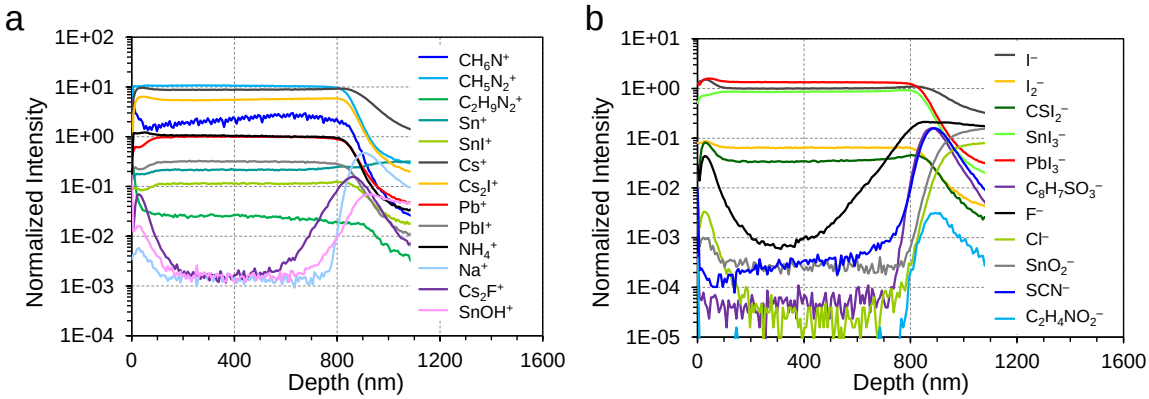

Fig. S2. ToF-SIMS depth profiles of the $EDAI_2$-treated perovskite film fabricated on an PEDOT:PSS/FTO-coated glass substrate, measured in **a,** positive and **b,** negative polarity.

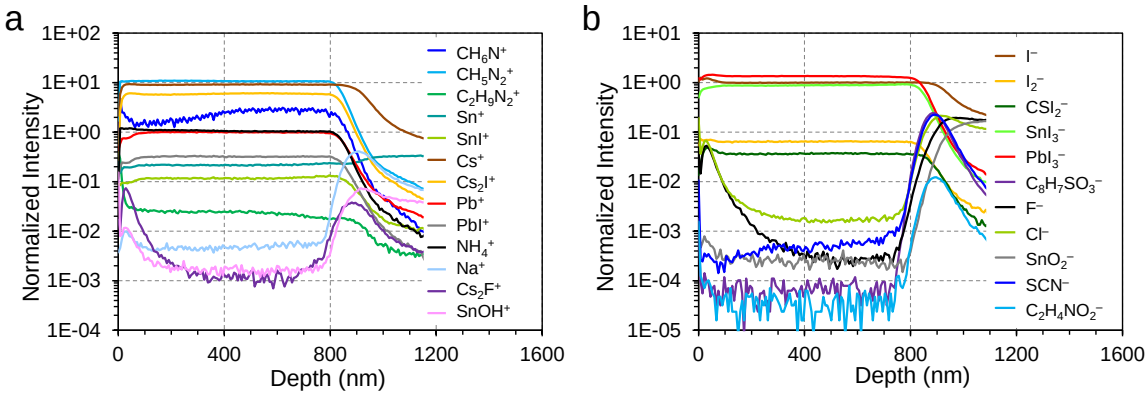

Fig. S3. ToF-SIMS depth profiles of the $EDAI_2$/GlyHCl-treated perovskite film fabricated on an PEDOT:PSS/FTO-coated glass substrate, measured in **a,** positive and **b,** negative polarity.

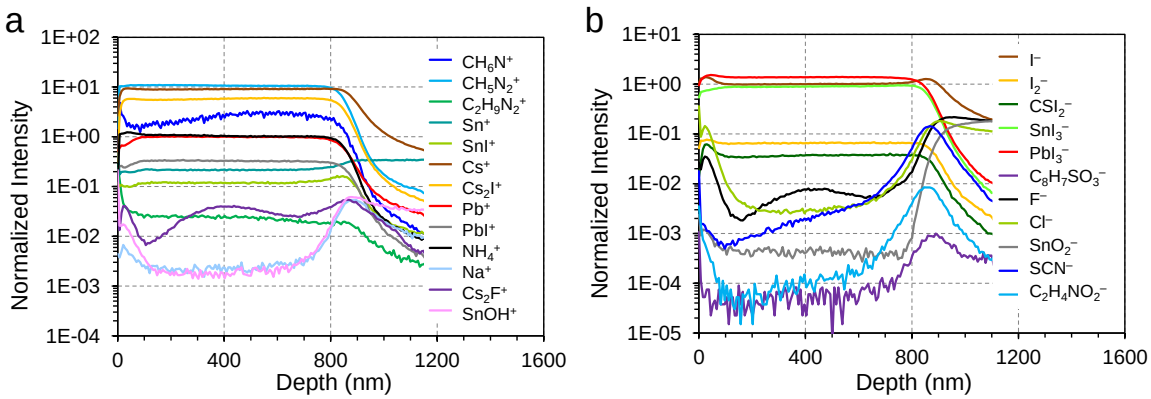

Fig. S4. ToF-SIMS depth profiles of the $EDAI_2$/GlyHCl-treated perovskite film fabricated on an FTO-coated glass substrate with no PEDOT:PSS layer, measured in **a,** positive and **b,** negative polarity.

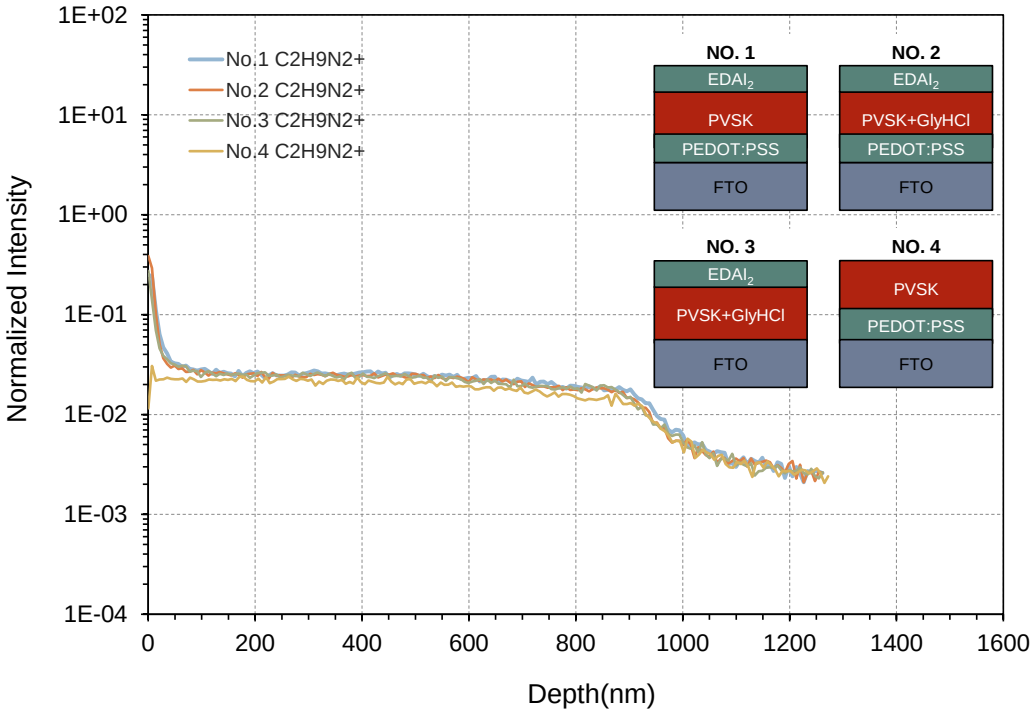

Fig. S5. ToF-SIMS depth profile of EDA^{2+} ions in the different perovskite films: No. 1 $EDAI_2$ -treated, No. 2 $EDAI_2$/GlyHCl-treated, No. 3 $EDAI_2$/GlyHCl-treated without PEDOT:PSS and No. 4 Control perovskite films.

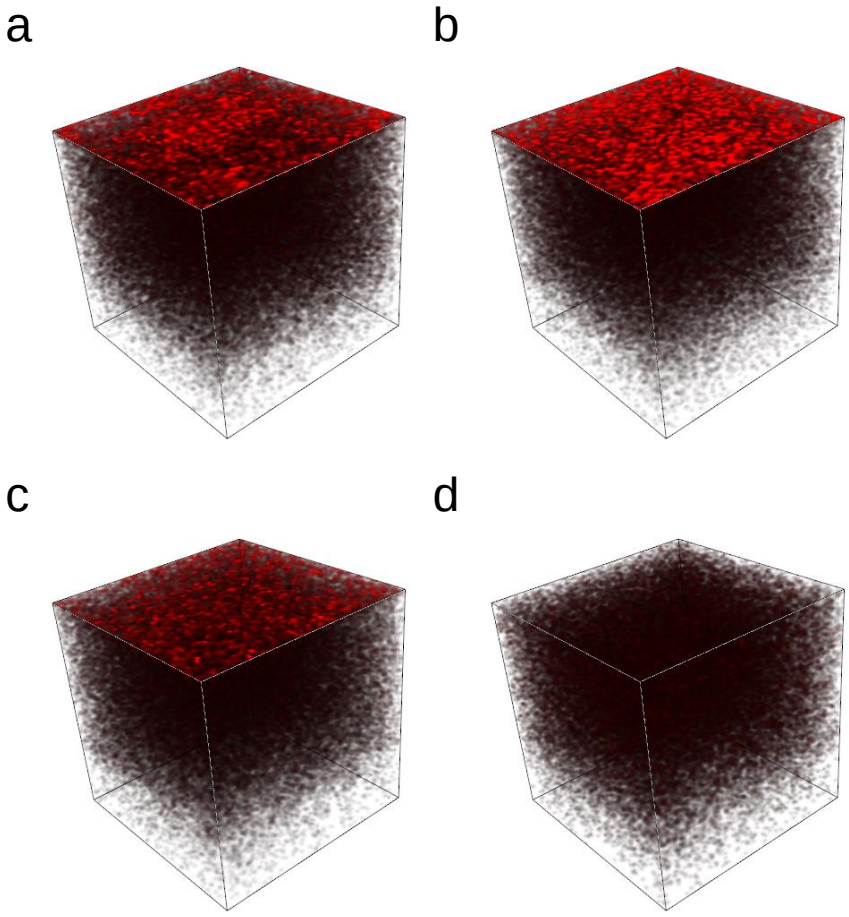

Fig. S6. Reconstructed 3D map (stretched in the z direction for clarity) showing the distributions of EDA^{2+} ions through the perovskite films without subtracting the background signals. **a,** $EDAI_2$-treated, **b,** $EDAI_2$/GlyHCl-treated, **c,** $EDAI_2$/GlyHCl-treated without PEDOT:PSS and **d,** Control perovskite films.

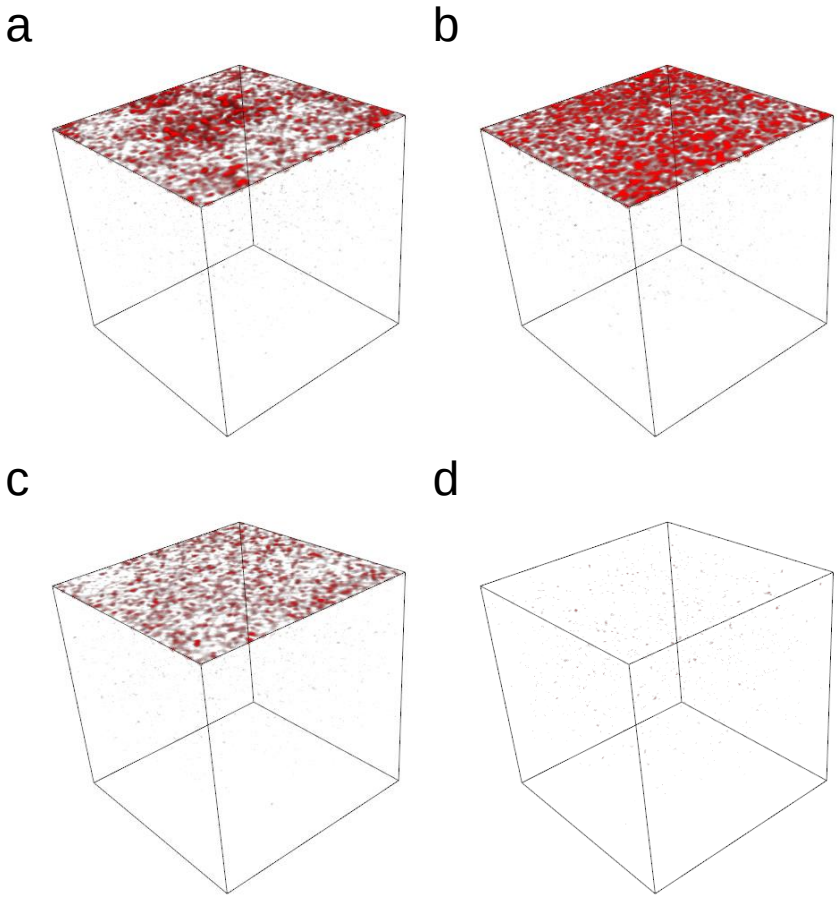

Fig. S7. Reconstructed 3D map (stretched in the z direction for clarity) showing the distributions of EDA^{2+} ions through the perovskite films after subtracting the background signals. **a,** $EDAI_2$-treated, **b,** $EDAI_2$/GlyHCl-treated, **c,** $EDAI_2$/GlyHCl-treated without PEDOT:PSS and **d,** Control perovskite films.

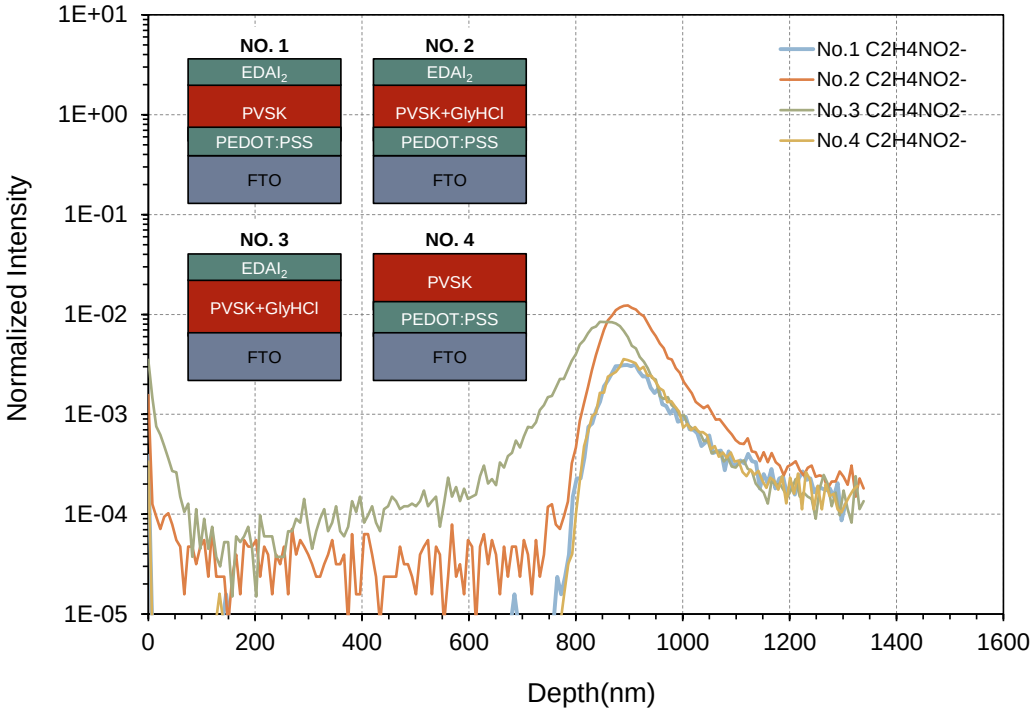

Fig. S8. ToF-SIMS depth profile of $GlyH^+$ ions in the perovskite films, inserted figures show the corresponding sample information. No. 1 $EDAI_2$-treated, No. 2 $EDAI_2$/GlyHCl-treated, No. 3 $EDAI_2$/GlyHCl-treated without PEDOT:PSS and No. 4 Control perovskite films.

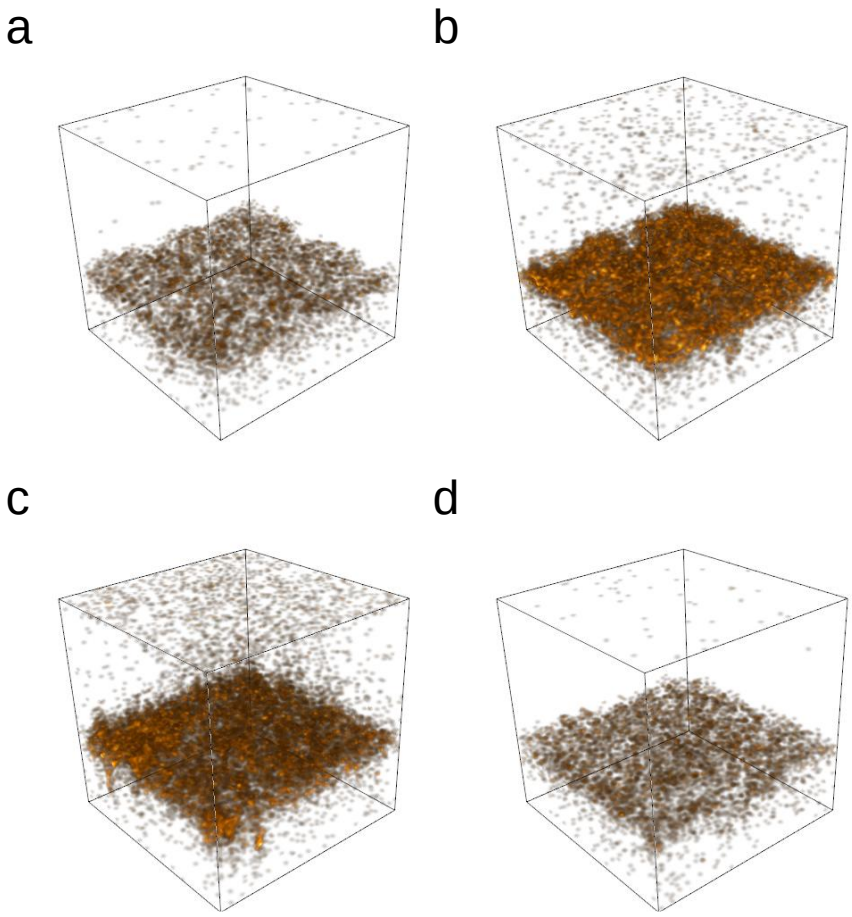

Fig. S9. Reconstructed 3D map (stretched in the z direction for clarity) showing the distributions of $GlyH^+$ ions through the perovskite films without subtracting the background signals. **a,** $EDAI_2$-treated, **b,** $EDAI_2$/GlyHCl-treated, **c,** $EDAI_2$/GlyHCl-treated without PEDOT:PSS and **d,** Control perovskite films.

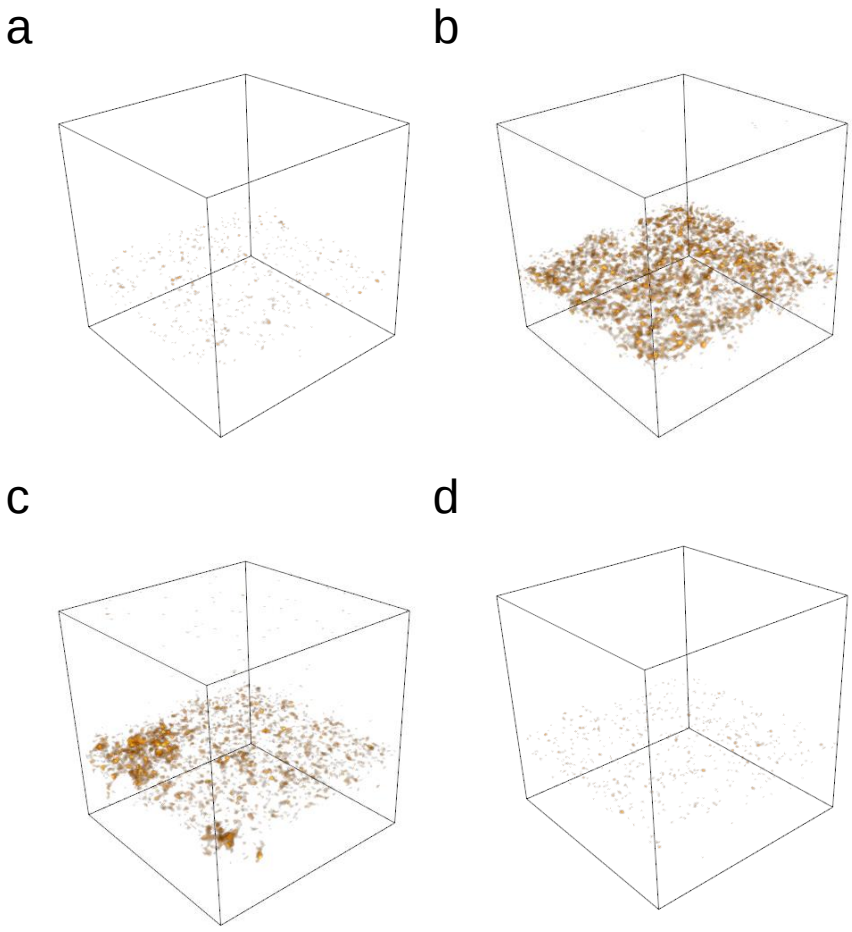

Fig. S10. Reconstructed 3D map (stretched in the z direction for clarity) showing the distributions of $GlyH^+$ ions through the perovskite films after subtracting the background signals. **a,** $EDAI_2$-treated, **b,** $EDAI_2$/GlyHCl-treated, **c,** $EDAI_2$/GlyHCl-treated without PEDOT:PSS and **d,** Control perovskite films.

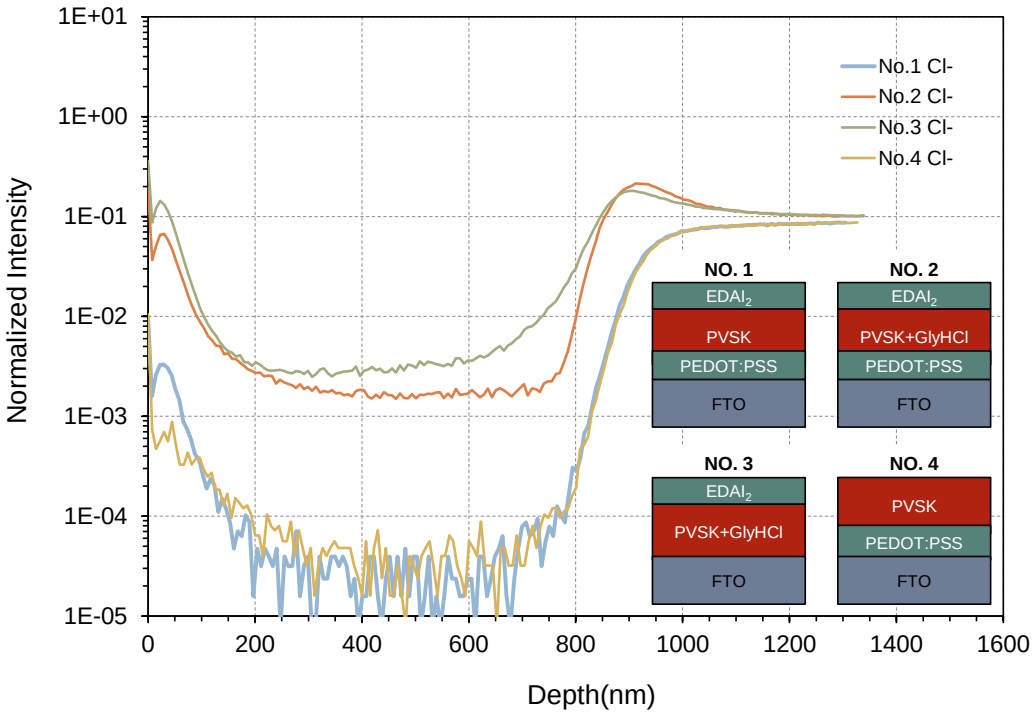

Fig. S11. ToF-SIMS depth profile of Cl^- ions in the perovskite films, inserted figures show the corresponding sample information. No. 1 $EDAI_2$-treated, No. 2 $EDAI_2$/GlyHCl-treated, No. 3 $EDAI_2$/GlyHCl-treated without PEDOT:PSS and No. 4 Control perovskite films.

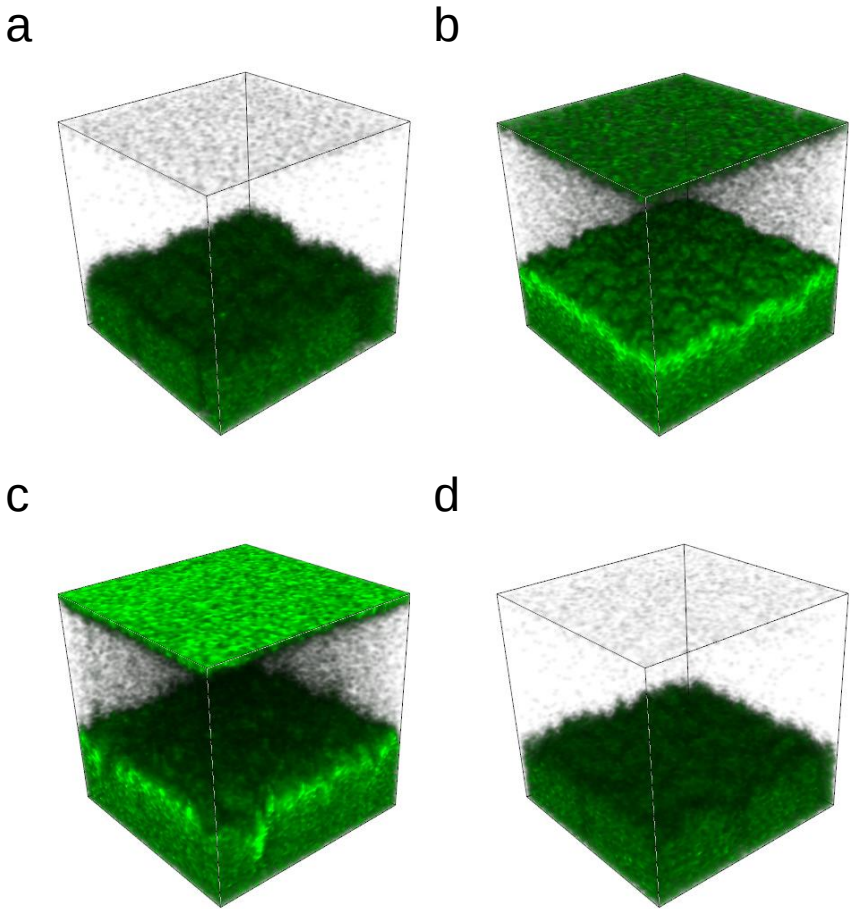

Fig. S12. Reconstructed 3D map (stretched in the z direction for clarity) showing the distributions of Cl^- ions through the perovskite films without subtracting the background signals. **a,** $EDAI_2$-treated, **b,** $EDAI_2$/GlyHCl-treated, **c,** $EDAI_2$/GlyHCl-treated without PEDOT:PSS and **d,** Control perovskite films.

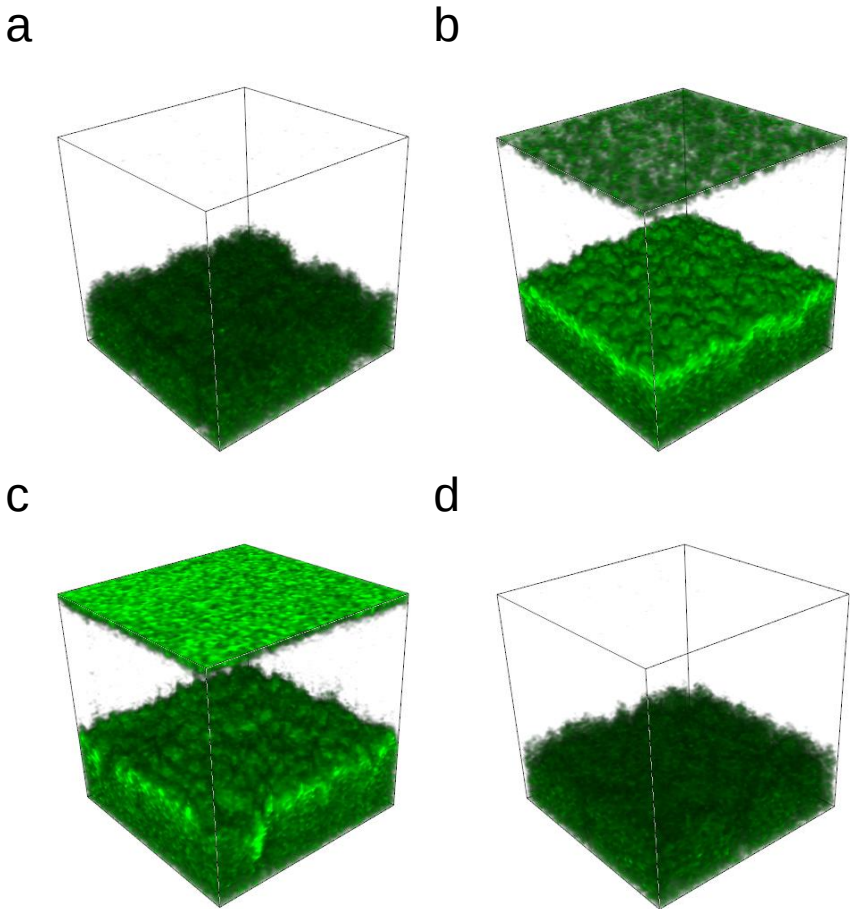

Fig. S13. Reconstructed 3D map (stretched in the z direction for clarity) showing the distributions of Cl^- ions through the perovskite films after subtracting the background signals. **a,** $EDAI_2$-treated, **b,** $EDAI_2$/GlyHCl-treated, **c,** $EDAI_2$/GlyHCl-treated without PEDOT:PSS and **d,** Control perovskite films.

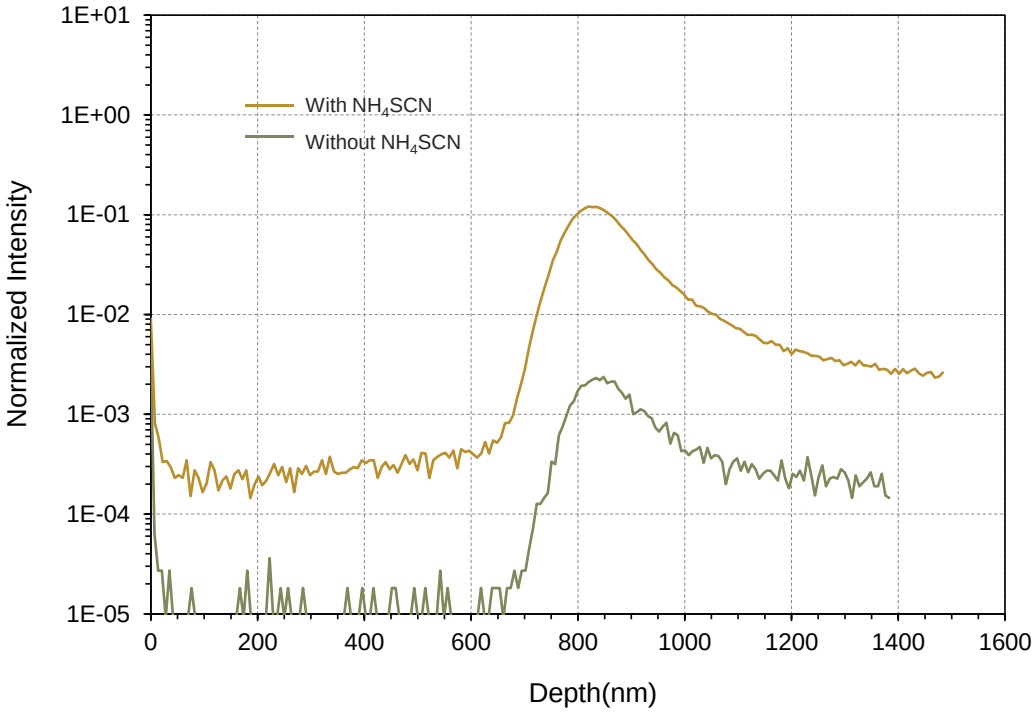

Fig. S14. ToF-SIMS depth profile of SCN^- ions in the perovskite films prepared with and without the addition of NH_4SCN.

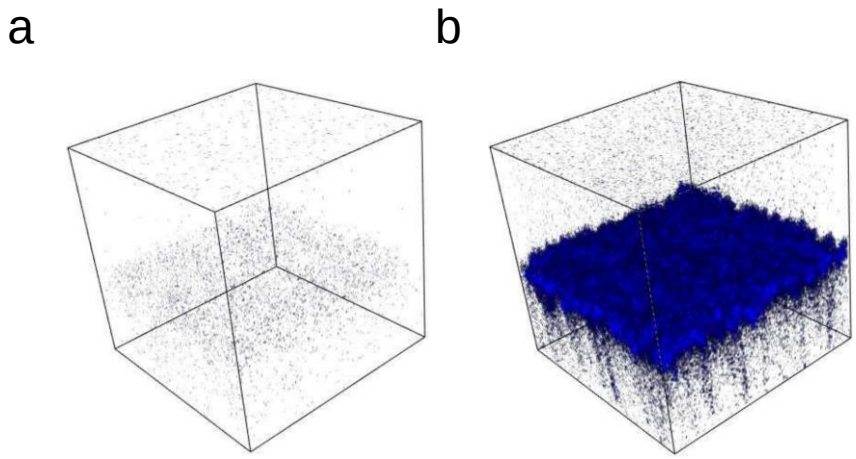

Fig. S15. Reconstructed 3D map (stretched in the z direction for clarity) showing the distributions of SCN^- ions in the perovskite films prepared with **a,** and without **b,** the addition of NH_4SCN.

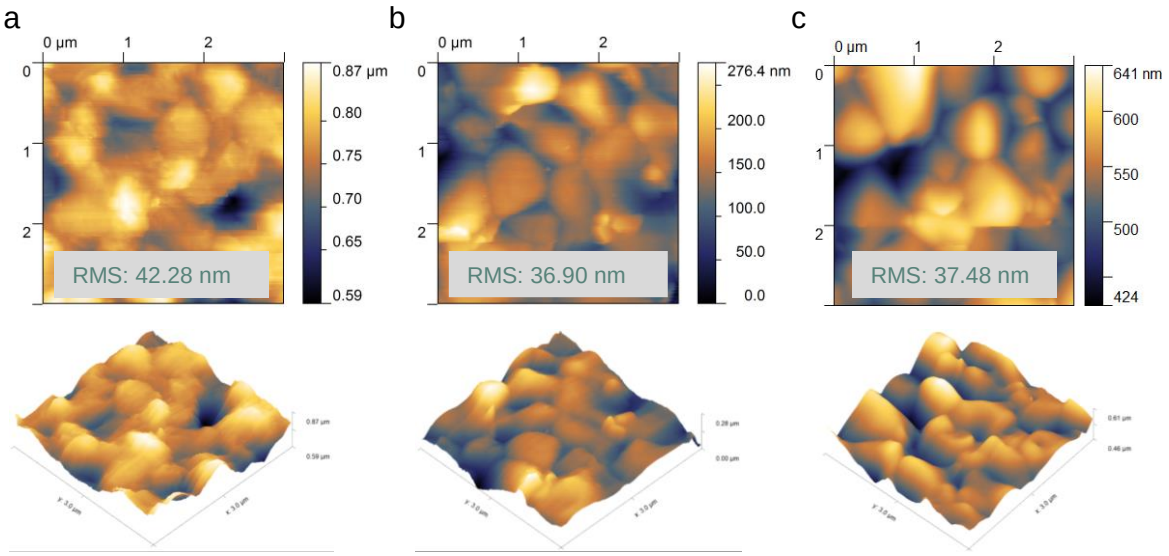

Fig. S16. AFM images of the **a,** control, **b,** $EDAI_2$-treated, and **c,** $EDAI_2$/GlyHCl-treated perovskite films.

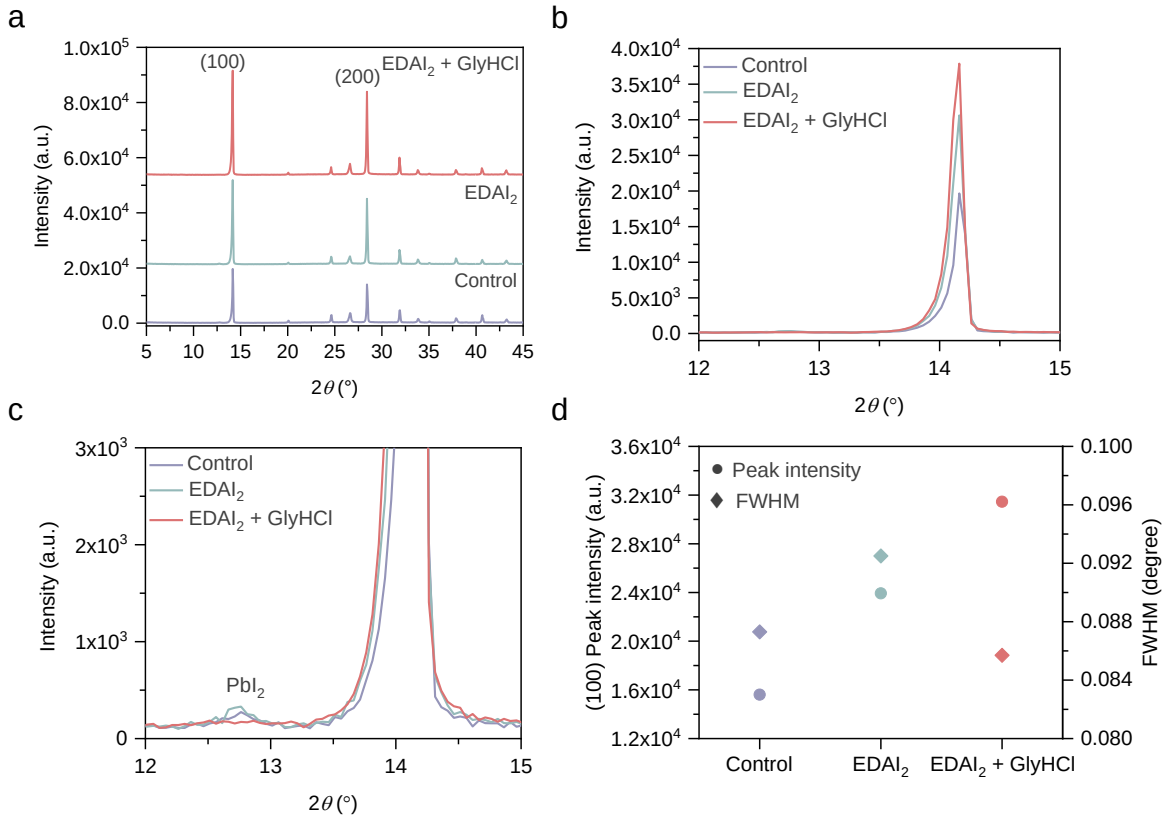

Fig. S17. XRD patterns of perovskite films with the 2θ range from **a,** 5° to 45°, **b,** 12° to 15° for showing the difference of the (100) peak intensity of the films, **c,** 12° to 15° with magnification for showing the PbI_2 peaks; **d,** the corresponding peak intensity and full width at half maximum (FWHM) of the (100) peaks. All diffraction peaks of fluorine-doped tin oxide (FTO) are indexed following the rutile tetragonal crystalline phase of SnO_2 (COD No. 96-210-1854). A thin layer of PMMA was coated onto the perovskite films to prevent oxidation.

To confirm the effect of GlyHCl on the enhancement of the film crystallinity, we also compared the XRD patterns of the films fabricated with the addition of 2, 4, and 8 mol% GlyHCl without $EDAI_2$ post-treatment (Fig. S18). The intensity of the (100) peak increases with the amount of GlyHCl added into the precursor solution, and no new peaks or peak-shifts can be observed. We can therefore conclude that GlyHCl enhances the crystallinity of the resultant perovskite films without inducing any new crystalline phases, such as the low dimension perovskite crystals for example.

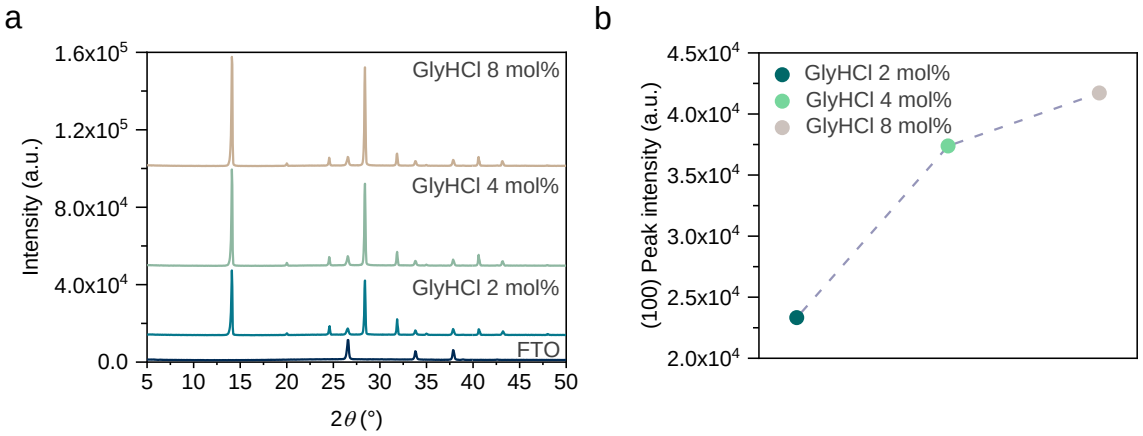

Fig. S18. a, XRD patterns of perovskite films prepared with the addition of 2, 4, and 8 mol% of GlyHCl (without $EDAI_2$ post-treatment); **b,** the corresponding peak intensity of the (100) peaks.

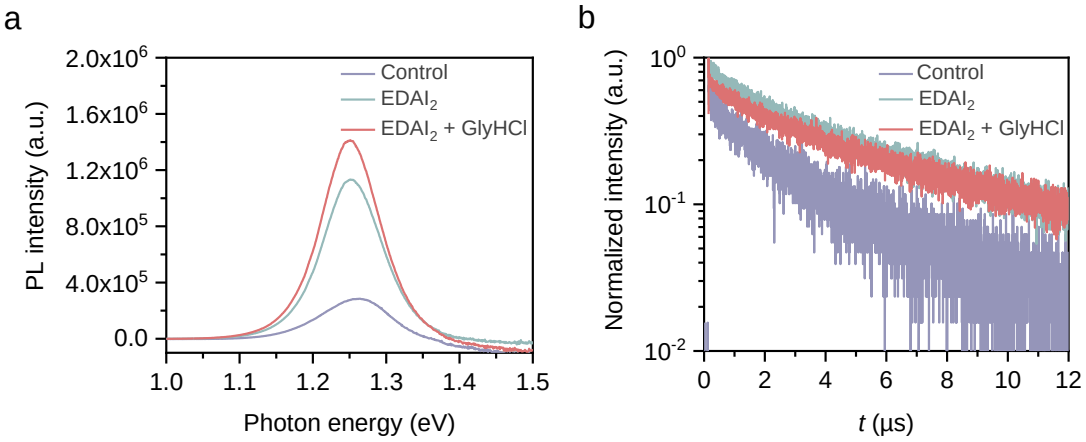

Fig. S19. a, Steady-state photoluminescence (PL) spectra of the perovskite films fabricated on quartz substrates with the front-side excitation. **b,** Time-resolved photoluminescence (TRPL) decay of the perovskite films fabricated on quartz substrates with the front-side excitation.

Table S1. The PL lifetimes and PL intensities of the perovskite films.

Front-side excitation (Film surface side)	PL lifetime (μs)	PL intensity ($\times 10^6$)
Control	2.8	2.8
$EDAI_2$	4.5	11.4
$EDAI_2$ + GlyHCl	4.9	14.1
Back-side excitation (Quartz side)	**PL lifetime (μs)**	**PL intensity ($\times 10^6$)**
Control	1.5	2.3
$EDAI_2$	3.2	13.0
$EDAI_2$ + GlyHCl	5.5	21.4

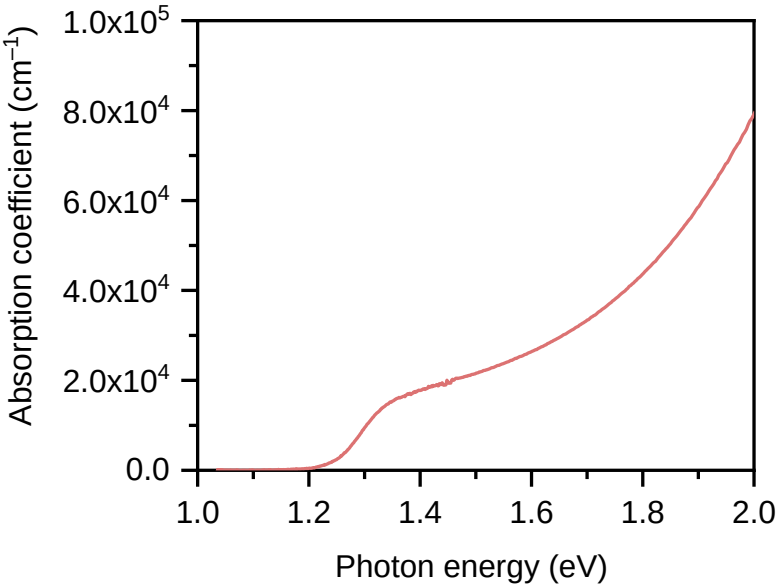

Fig. S20. Optical absorption spectrum of the $EDAI_2$/GlyHCl-treated perovskite film on quartz substrate.

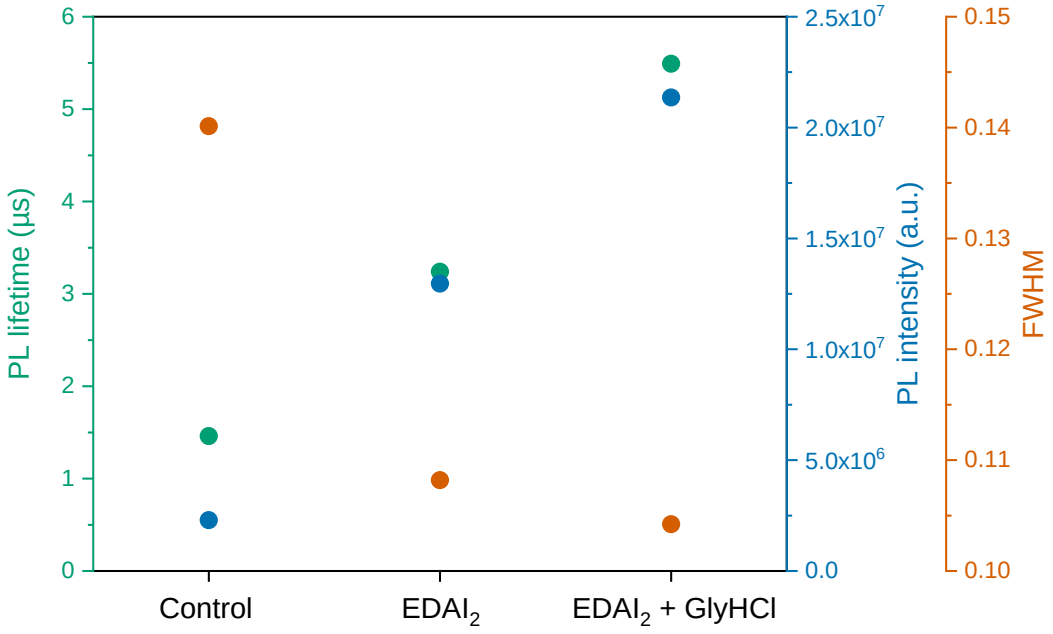

Fig. S21. The PL lifetime, PL intensity, and FWHM of the PL peaks for the perovskite films fabricated on the quartz substrates with the back-side excitation.

At the range of excitation intensities under consideration here, the dependences of PL decay curves, PL lifetimes, and initial PL intensities shown in Fig. 2c, d, S22 are well explained by a simple rate equation that includes single-carrier trapping and two-carrier (electron−hole) radiative recombination[3]:

$$\frac{dn}{dt} = -An - Bn^2 \tag{1}$$

$$I_{\mathrm{PL}} \propto BnN + Bn^2 \tag{2}$$

Here n and I_{PL} are the photoexcited carrier density and the PL intensity, respectively. A, B, and N are the carrier trapping rate, the two-carrier radiative recombination coefficient, and the unintentional doped carrier density, respectively. Note that photoexcitation produces equal numbers of electrons and holes. The initial photoexcited carrier density $n(t = 0) = n_0$ is given as follows:

$$n_0 = \alpha F_{\mathrm{ex}} = \frac{\alpha\lambda}{hc} I_{\mathrm{ex}} \tag{3}$$

Here h, c, λ, α, I_{ex}, and F_{ex} are the Planck constant, the speed of light, the excitation wavelength, the absorption coefficient at the excitation wavelength, the excitation fluence, and the excitation photon flux, respectively. In our TR-PL experiments, λ = 688 nm and α = 4.4×10^4 cm^{-1}. The excitation fluence of I_{ex} = 100 nJ cm^{-2} corresponds to $n_0 = 1.5 \times 10^{16}$ cm^{-3} and $F_{\mathrm{ex}} = 3.5 \times 10^{11}$ photons/cm^2, comparable to the incident photon flux under AM 1.5G.

By solving the rate equations, the time-dependent PL intensity can be obtained as follows:

$$I_{\mathrm{PL}}(t) = I_0 \left(\frac{N}{N + n_0} \left(\frac{n(t)}{n_0} \right) + \frac{n_0}{N + n_0} \left(\frac{n(t)}{n_0} \right)^2 \right) \tag{4}$$

where

$$\frac{n(t)}{n_0} = \frac{e^{-At}}{1 + \frac{Bn_0}{A}(1 - e^{-At})} \tag{5}$$

and

$$I_0 = \xi(N + n_0)n_0 \quad (6)$$

Here, I_0 is the initial PL intensity, while ξ is a constant that dependent on several factors, including the detection efficiency and the charge carrier extraction efficiency. According to the global fitting using Eqs. (4)–(6), $A = 9.2 \times 10^4$ s^{-1}, $B = 2.0 \times 10^{-11}$ cm^{3}s^{-1}, and $N = 8.2 \times 10^{14}$ cm^{-3} are obtained for the GlyHCl/EDAI$_2$-treated sample. The value of A is three orders of magnitude lower than that of MAPbI$_3$[3], suggesting that our films have a lower density of traps such as the structural defects and impurities. The value of B is one order of magnitudes lower than that of MAPbI$_3$[3], probably because of the smaller bandgap energy of Sn–Pb perovskites. The obtained unintentionally-doped carrier density N is similar to the reported values of MAPbI$_3$ (~10^{15} cm^{-3})[3], suggesting that the characteristic p-doping commonly observed in Sn-containing perovskite materials is largely suppressed in our GlyHCl/EDAI$_2$-treated mixed Sn–Pb perovskite films.

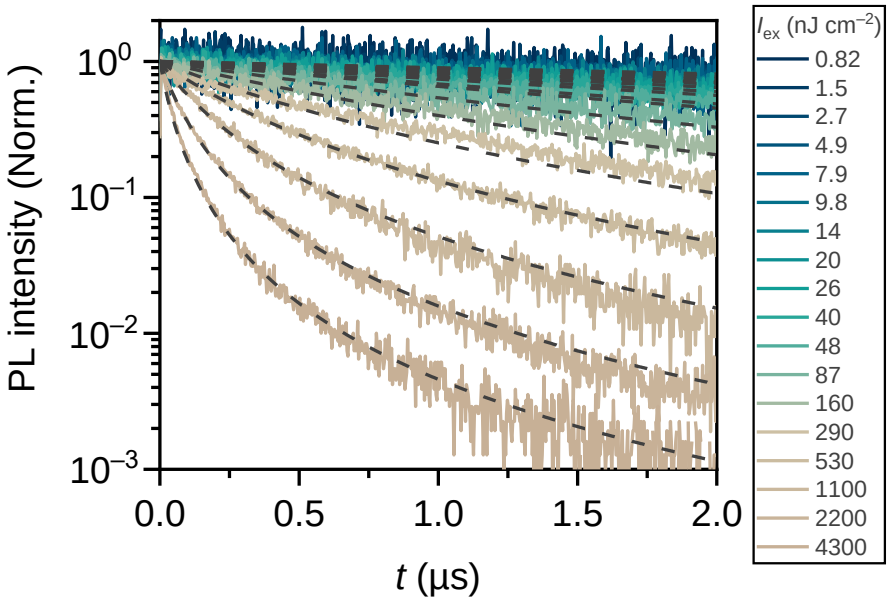

Fig. S22. PL dynamics of the EDAI$_2$/GlyHCl-treated films under different excitation intensities. Dashed lines represent the fit of the decay signals to the rate equations reported in our previous work[3].

Space-charge-limited currents (SCLC) measurement

Trap densities in the perovskite films were estimated from dark current−voltage ($I-V$) curves obtained for FTO/PEDOT:PSS/perovskite/PTAA/Ag hole-only, and FTO/C_{60}/perovskite/C_{60}/Ag electron-only devices[4,5]. Fig. S23 shows the $I-V$ curves of the hole-only devices. The voltages where the currents start to sharply increase can be assigned to the trap-filled limit voltage (V_{TFL}), from which the trap density, N_{trap}, can be estimated using the following relation: $V_{TFL} = N_{trap}(eL^2)/(2\varepsilon_r\varepsilon_0)$, where e is the elementary charge of the electron, ε_0 is the vacuum permittivity, ε_r is the relative dielectric constant of the perovskite (around 32)[6], and L is the thickness of the perovskite film. The V_{TFL} values are given in Table S2. The estimated trap densities for the control, $EDAI_2$-treated, and $EDAI_2$/GlyHCl-treated films were 3.0×10^{15}, 2.9×10^{15}, and 1.7×10^{15} cm^{-3}, respectively. The $EDAI_2$/GlyHCl-treated films have the lowest trap-state density, and therefore, the corresponding devices should have the smallest number of recombination events. Meanwhile, the $EDAI_2$/GlyHCl-treated films also showed a low density of electron traps (2.9×10^{14} cm^{-3}), as determined from the electron only devices.

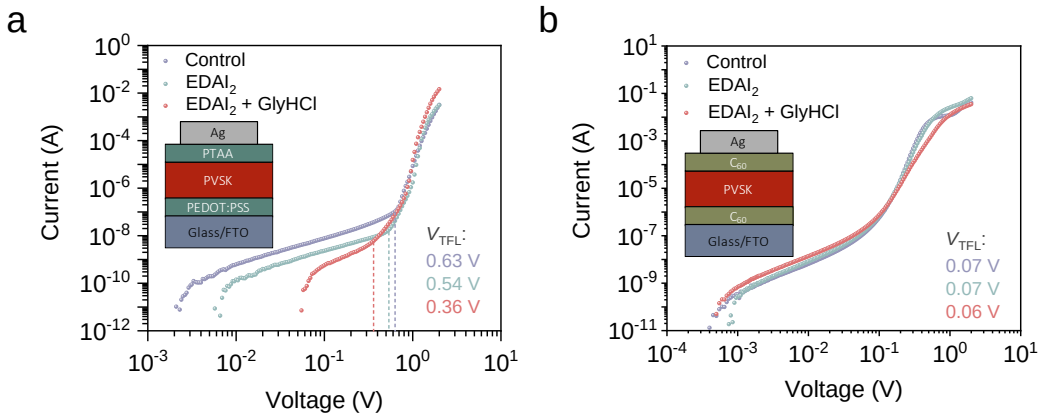

Fig. S23. Dark *J*–*V* curves of the **a,** hole-only and **b,** electron-only devices with the architectures of FTO/PEDOT:PSS/perovskite/PTAA/Ag and FTO/C_{60}/perovskite/C_{60}/Ag, respectively.

Table S2. The hole and electron trap densities estimated from the SCLC measurements.

Sample	Hole-only devices		N_{trap} (hole) (cm^{-3})	Electron-only devices		N_{trap} (electron) (cm^{-3})
	Thickness (nm)	V_{TFL} (V)		Thickness (nm)	V_{TFL} (V)	
Control	867	0.63	3.0×10^{15}	817	0.07	3.7×10^{14}
$EDAI_2$	814	0.54	2.9×10^{15}	775	0.07	3.9×10^{14}
$EDAI_2$ + GlyHCl	863	0.36	1.7×10^{15}	828	0.06	2.9×10^{14}

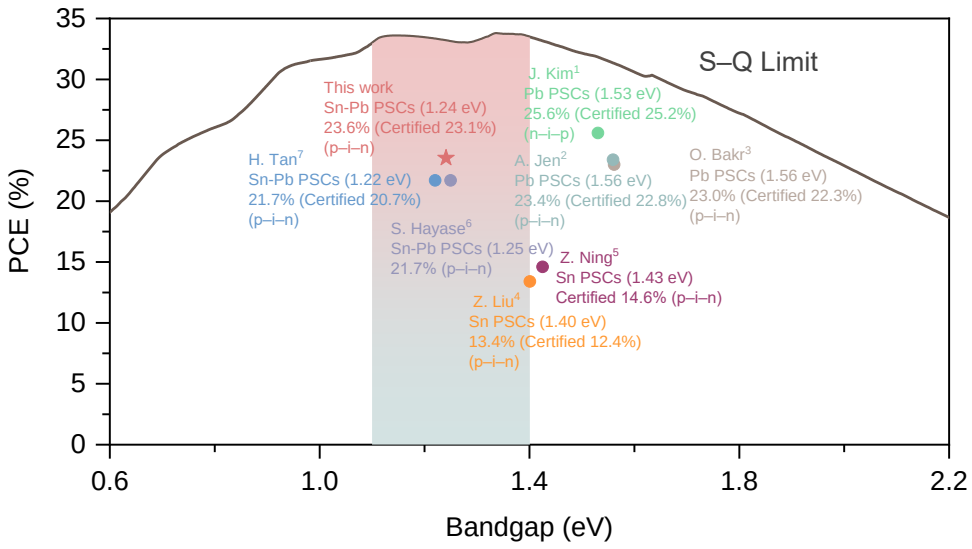

Fig. S24. Efficiencies of some representative PSCs. The bandgap from 1.1 to 1.4 eV is the optimal range for a single junction solar cell based on Shockley–Queisser theory[7]. Plotted PCEs are referred from **1**: J. Kim et al., *Nature* **2021**, *592*, 381–385. Perovskite composition: α-$FAPbI_3$; **2**: A. K.-Y. Jen et al., *J. Am. Chem. Soc.* **2020**, *142*, 20134–20142. Perovskite composition: $Cs_{0.05}(FA_{0.95}MA_{0.05})_{0.95}Pb(I_{0.95}Br_{0.05})_3$; **3:** O. Bakr et al., *Nat. Energy* **2020**, *5*, 131–140. Perovskite composition: $Cs_{0.05}(FA_{0.92}MA_{0.08})_{0.95}Pb(I_{0.92}Br_{0.08})_3$; **4:** Z. Liu at al., *Matter* **2021**, *4*, 709–721. Perovskite composition: $FASnI_{2.9}Br_{0.1}$; **5:** Z. Ning et al., *J. Am. Chem. Soc.* **2021**, DOI: 10.1021/jacs.1c03032. Perovskite composition: 2D/3D tin perovskite; **6:** S. Hayase et al., *Adv. Energy Mater.* **2021**, DOI: 10.1002/aenm.202101069. Perovskite composition: $Cs_{0.025}FA_{0.475}MA_{0.5}Sn_{0.5}Pb_{0.5}I_{2.975}Br_{0.025}$; **7:** H. Tan et al., *Nat. Energy* **2020**, *5*, 870–880. Perovskite composition: $FA_{0.7}MA_{0.3}Pb_{0.5}Sn_{0.5}I_3$.

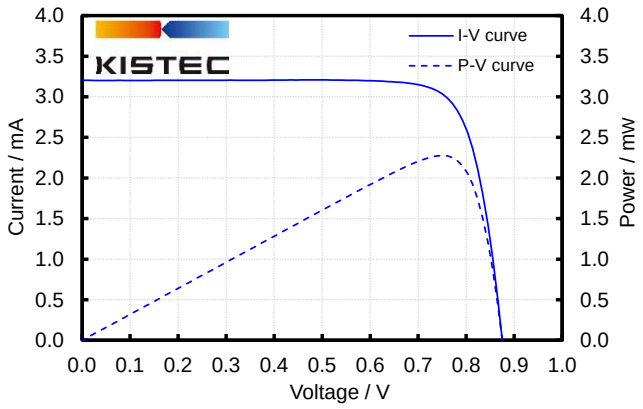

Date : 11 Mar 2021
Cell name : HF2714-Right
Start delay time : 100 ms
Delay time : 10 ms
Integration time : 10 ms
Sweep direction : Reverse
Designated area : 0.0985 cm^2
Isc : 3.203 / mA
Voc : 0.875 / V
Pmax : 2.278 / mW
Ipm : 3.039 / mA
Vpm : 0.750 / V
F.F. : 81.2 / %
Eff. : 23.1 / %
M. Temp : R.T.

I-V curve and P-V curve

Fig. S25. Certification data of an unencapsulated sample cell (Reverse scan), measured by the Kanagawa Institute of Industrial Science and Technology (KISTEC).

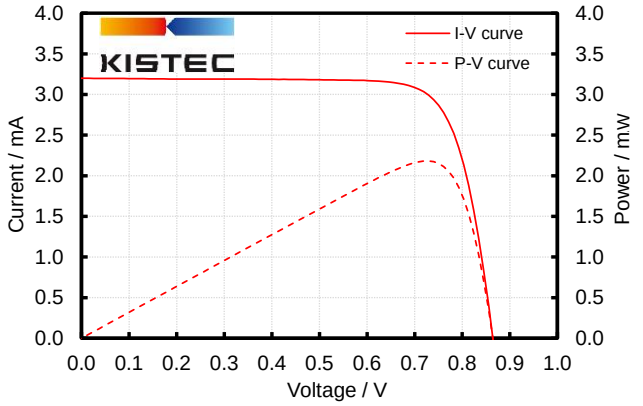

Date : 11 Mar 2021
Cell name : HF2714-Right
Start delay time : 100 ms
Delay time : 10 ms
Integration time : 10 ms
Sweep direction : Forward
Designated area : 0.0985 cm^2
Isc : 3.200 / mA
Voc : 0.864 / V
Pmax : 2.183 / mW
Ipm : 3.009 / mA
Vpm : 0.725 / V
F.F. : 79.0 / %
Eff. : 22.2 %
M. Temp : R.T.

I-V curve and P-V curve

Fig. S26. Certification data of an unencapsulated sample cell (Forward scan), measured by the Kanagawa Institute of Industrial Science and Technology (KISTEC).

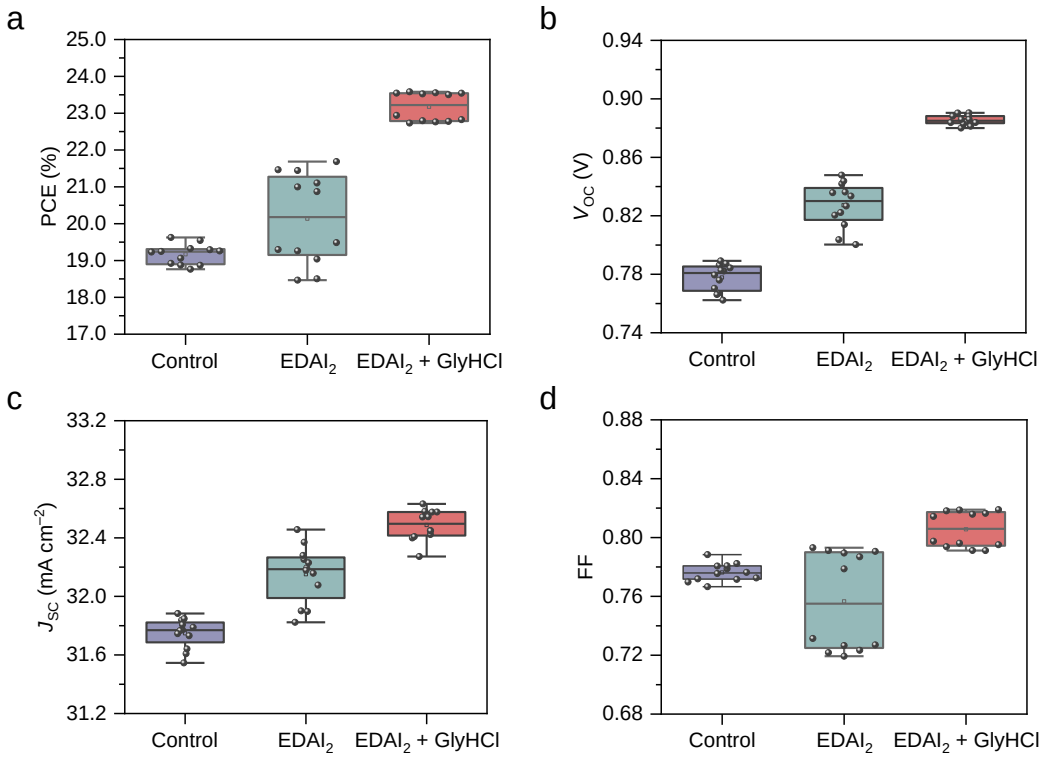

Fig. S27. Distribution of the device parameters derived from forward and reverse *J–V* scans for the control, $EDAI_2$-treated, and $EDAI_2$/GlyHCl-treated devices (six samples for each condition).

Table S3. Device performance parameters.

Sample	Scan[a]	J_{SC} (mA cm^{-2})	V_{OC} (V)	FF	PCE (%)
Control	Forward	31.6	0.76	0.78	18.8
	Reverse	31.6	0.78	0.78	19.3
	Forward	31.8	0.77	0.78	19.1
	Reverse	31.8	0.79	0.78	19.5
	Forward	31.8	0.77	0.78	18.9
	Reverse	31.6	0.79	0.79	19.6
	Forward	31.8	0.77	0.77	18.9
	Reverse	31.8	0.78	0.77	18.9
	Forward	31.9	0.78	0.78	19.3
	Reverse	31.8	0.78	0.77	19.3
	Forward	31.9	0.78	0.77	19.3
	Reverse	31.7	0.79	0.77	19.2
$EDAI_2$	Forward	32.2	0.81	0.73	19.0
	Reverse	32.2	0.83	0.78	20.9
	Forward	31.9	0.80	0.72	18.5
	Reverse	31.8	0.84	0.79	21.0
	Forward	32.1	0.80	0.72	18.5
	Reverse	31.9	0.84	0.79	21.1
	Forward	32.5	0.82	0.72	19.3
	Reverse	32.4	0.84	0.79	21.4
	Forward	32.2	0.83	0.73	19.5
	Reverse	32.3	0.85	0.79	21.7
	Forward	32.3	0.82	0.73	19.3
	Reverse	32.2	0.84	0.79	21.5
$EDAI_2$ + GlyHCl	Forward	32.5	0.88	0.79	22.8
	Reverse	32.4	0.89	0.82	23.6
	Forward	32.4	0.88	0.80	22.8
	Reverse	32.3	0.89	0.82	23.5
	Forward	32.6	0.88	0.79	22.8
	Reverse	32.4	0.89	0.82	23.5
	Forward	32.5	0.88	0.79	22.7
	Reverse	32.5	0.89	0.82	23.6
	Forward	32.6	0.88	0.80	22.8
	Reverse	32.5	0.89	0.82	23.5
	Forward	32.6	0.88	0.80	22.9
	Reverse	32.6	0.89	0.81	23.5

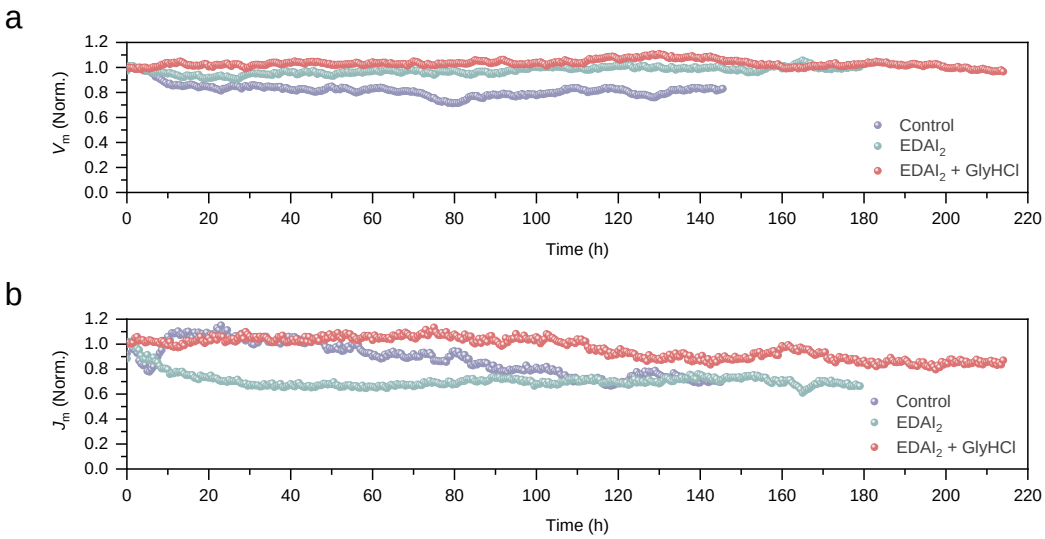

Fig. S28. Output voltages, **a,** and currents, **b,** obtained during the maximum power point tracking (MPPT) experiment condition for the control, $EDAI_2$-treated, and $EDAI_2$/GlyHCl-treated cells measured without encapsulation in a N_2-filled glovebox under AM 1.5G simulated solar illumination. The loss of PCE over time is mainly caused by the drop of output current, the output voltages remain relatively stable.

Table S4. Device performance parameters of nine large area PSCs with 1 cm^2 active device area.

Scan[a]	J_{SC} (mA cm^{-2})	V_{OC} (V)	FF	PCE (%)
Forward	32.02	0.88	0.70	19.7
Reverse	31.6	0.87	0.69	19.1
Forward	31.8	0.87	0.69	19.2
Reverse	31.5	0.87	0.68	18.5
Forward	32.2	0.88	0.68	19.1
Reverse	31.9	0.87	0.67	18.5
Forward	32.0	0.88	0.70	19.6
Reverse	31.5	0.87	0.69	19.0
Forward	33.1	0.88	0.72	21.0
Reverse	32.4	0.88	0.72	20.3
Forward	32.2	0.88	0.73	20.5
Reverse	31.6	0.87	0.72	19.8
Forward	32.1	0.88	0.72	20.3
Reverse	31.5	0.87	0.71	19.6
Forward	32.5	0.88	0.72	20.6
Reverse	31.6	0.88	0.72	19.9
Forward	33.7	0.87	0.67	19.6
Reverse	31.5	0.86	0.75	20.4

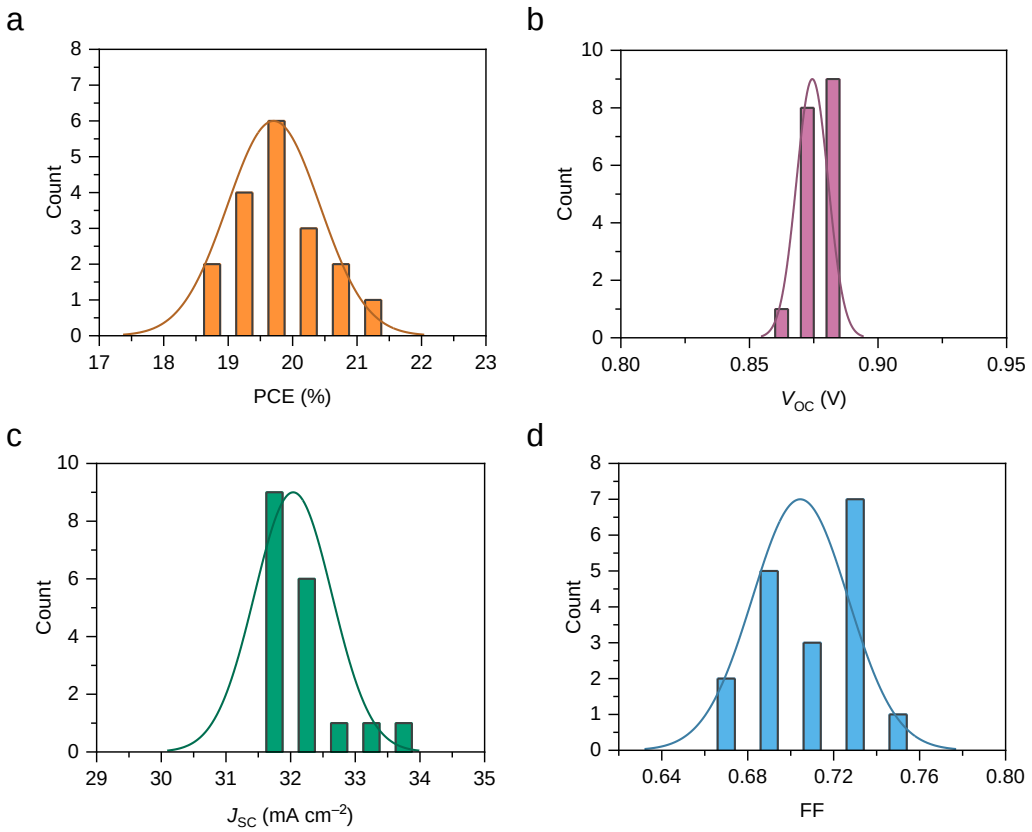

Fig. S29. Histograms of the *J–V* parameters obtained from nine large area devices with 1 cm^2 active area.

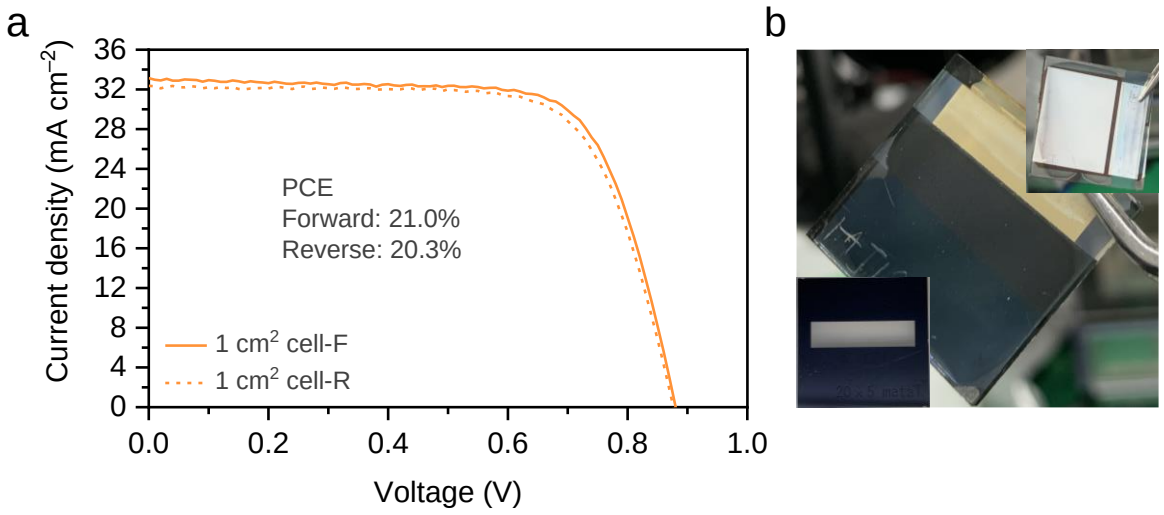

Fig. S30. a, *J*–*V* curves for the best performing large area device, with an active area 1 cm^2. The PCE is 21.0% for the forward scan (J_{SC} = 33.1 mA cm^{-2}, V_{OC} = 0.88 V, FF = 0.72). **b,** Photos of the cell with 1 cm^2 active area. Insets show the front side of the cell and the optical mask used for the measurement.

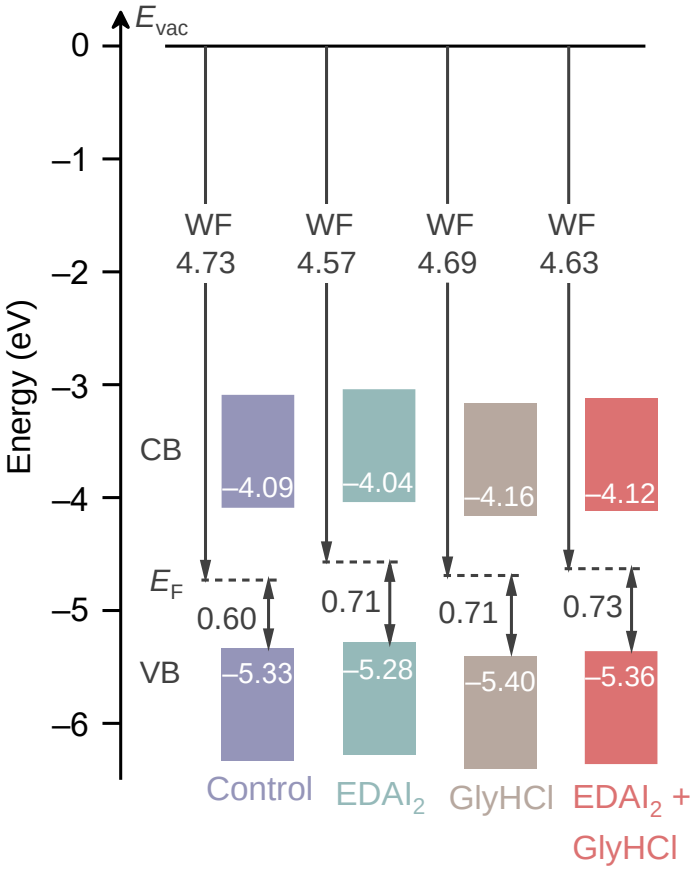

Fig. S31. Energy levels of the perovskite films. Energies are given in electron volts.

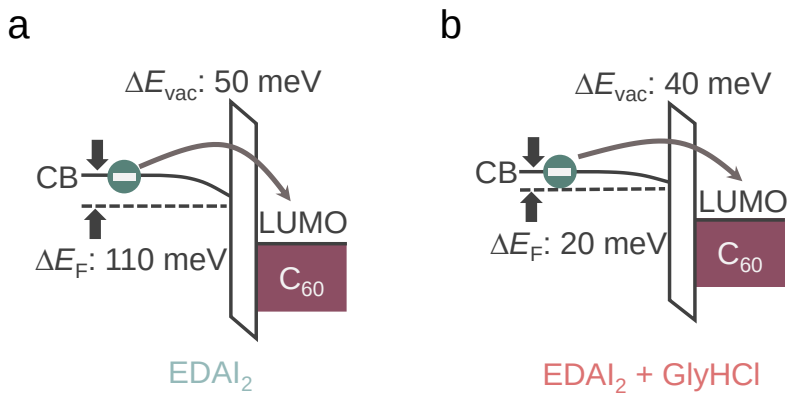

Fig. S32. Energy level shifts induced by $EDAI_2$ post-treatment for the perovskite layers prepared **a**, without GlyHCl additive and **b**, with GlyHCl additive.

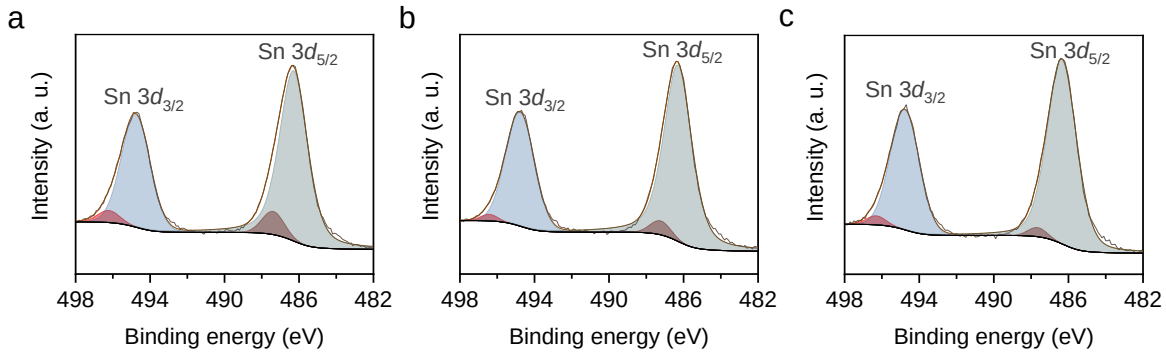

Fig. S33. XPS spectra of the Sn $3d_{3/2}$ and $3d_{5/2}$ core levels for the **a,** control, **b,** $EDAI_2$-treated, and **c,** $EDAI_2$/GlyHCl-treated perovskite films.

Table S5. The Sn^{4+}/Sn ratio and binding energy of the Sn^{4+} and Sn^{2+} peaks, as determined from the deconvolution of the $3d_{3/2}$ and $3d_{5/2}$ XPS peak manifolds shown in Fig. S32.

Sample	Sn^{4+}/Sn (%)	$3d_{3/2}$ (Binding energy, eV)		$3d_{5/2}$ (Binding energy, eV)	
		Sn^{4+}	Sn^{2+}	Sn^{4+}	Sn^{2+}
Control	8.5	496.23	494.77	487.39	486.29
$EDAI_2$	4.1	496.43	494.78	487.24	486.30
$EDAI_2$ + GlyHCl	3.9	496.32	494.77	487.66	486.35

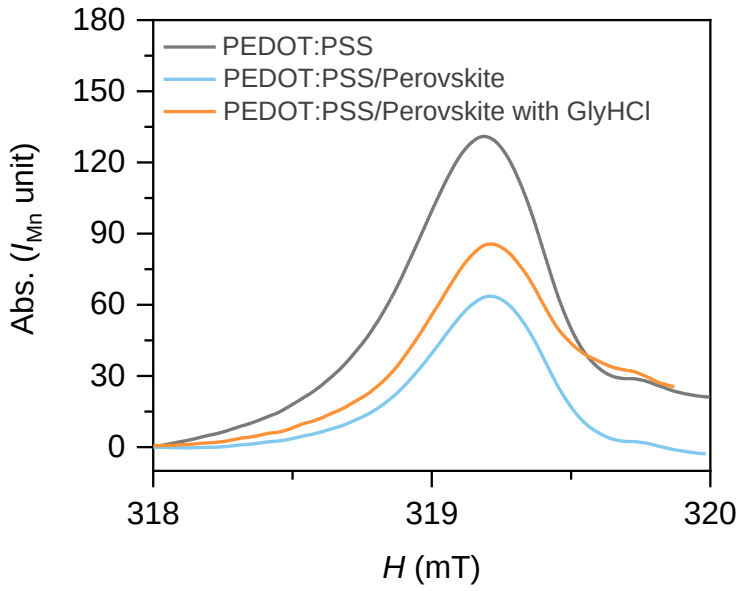

Fig. S34. The integrated ESR spectra for the data presented in Fig 4d.

Table S6. The number of spins and spin densities for the three PEDOT:PSS samples.

Sample[a]	No. of spins	Spin density (cm^{-3})
PEDOT:PSS	3.60×10^{13}	2.22×10^{19}
PEDOT:PSS/Perovskite	2.21×10^{13}	1.36×10^{19}
PEDOT:PSS/Perovskite + GlyHCl	2.39×10^{13}	1.47×10^{19}

[a]The films were fabricated on quartz substrates.

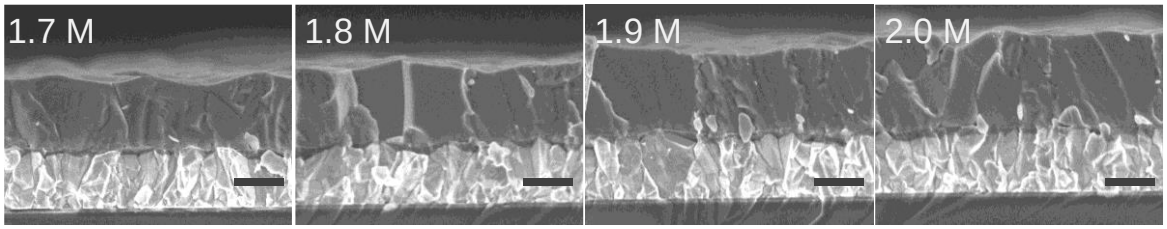

Fig. S35. Cross-sectional SEM images (scale bar: 500 nm) of the $EDAI_2$/GlyHCl-treated perovskite films fabricated using precursor solutions with concentrations of 1.7, 1.8, 1.9 and to 2.0 M.

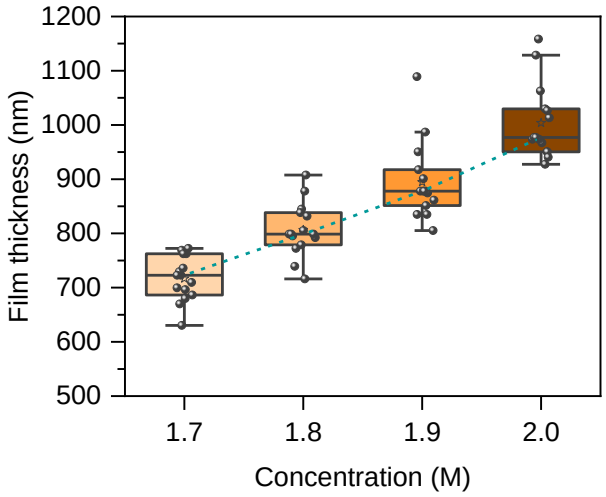

Fig. S36. Variation in film thickness with perovskite precursor concentration. The average thickness of the perovskite films is 720, 810, 895, and 1000 nm for the precursor concentration of 1.7, 1.8, 1.9, and 2.0 M, respectively.

Table S7. Device performance parameters of $EDAI_2$/GlyHCl-treated PSCs fabricated with different concentrations of the precursor solution.

Concentration (M)	Scan[a]	J_{SC} (mA cm^{-2})	V_{OC} (V)	FF	PCE (%)
1.7	Forward	33.5	0.84	0.76	21.6
	Reverse	33.3	0.84	0.79	22.0
	Forward	33.5	0.84	0.77	21.7
	Reverse	33.2	0.84	0.78	21.8
	Forward	33.5	0.85	0.76	21.5
	Reverse	32.9	0.84	0.79	22.0
	Forward	33.4	0.84	0.77	21.4
	Reverse	33.1	0.82	0.78	21.2
	Forward	33.2	0.83	0.77	21.1
	Reverse	32.9	0.82	0.77	20.9
	Forward	33.1	0.83	0.77	21.1
	Reverse	32.7	0.82	0.78	20.8
1.8	Forward	33.6	0.84	0.75	21.1
	Reverse	33.2	0.83	0.79	21.9
	Forward	33.5	0.83	0.75	20.9
	Reverse	33.0	0.83	0.78	21.4
	Forward	33.3	0.84	0.74	20.6
	Reverse	33.0	0.83	0.78	21.3
	Forward	33.6	0.83	0.77	21.5
	Reverse	33.3	0.83	0.78	21.5
	Forward	33.5	0.84	0.76	21.4
	Reverse	33.0	0.83	0.79	21.8
	Forward	33.4	0.85	0.76	21.4
	Reverse	33.1	0.84	0.79	22.0
1.9	Forward	33.3	0.85	0.74	20.9
	Reverse	32.7	0.84	0.79	21.9
	Forward	33.5	0.85	0.75	21.3
	Reverse	33.0	0.84	0.79	21.8
	Forward	33.5	0.85	0.76	21.6
	Reverse	33.2	0.84	0.78	21.7
	Forward	33.4	0.84	0.76	21.5
	Reverse	32.9	0.84	0.79	21.7
	Forward	33.3	0.85	0.76	21.6

	Reverse	33.0	0.84	0.79	21.9
	Forward	33.5	0.85	0.74	21.1
	Reverse	32.5	0.85	0.80	21.9
	Forward	33.5	0.85	0.73	20.8
	Reverse	32.6	0.85	0.79	21.9
	Forward	33.2	0.85	0.74	20.9
	Reverse	32.3	0.85	0.80	21.9
	Forward	33.1	0.86	0.71	20.4
	Reverse	31.8	0.86	0.80	22.0
2.0	Forward	33.5	0.84	0.77	21.6
	Reverse	33.1	0.84	0.79	21.8
	Forward	33.4	0.85	0.76	21.5
	Reverse	33.0	0.84	0.79	22.0
	Forward	33.4	0.85	0.75	21.2
	Reverse	32.5	0.85	0.80	22.0
	Forward	33.5	0.84	0.73	20.7
	Reverse	32.5	0.84	0.79	21.8
	Forward	33.0	0.85	0.74	20.7
	Reverse	32.3	0.84	0.80	21.9
	Forward	32.6	0.84	0.71	19.5
	Reverse	31.3	0.85	0.81	21.5

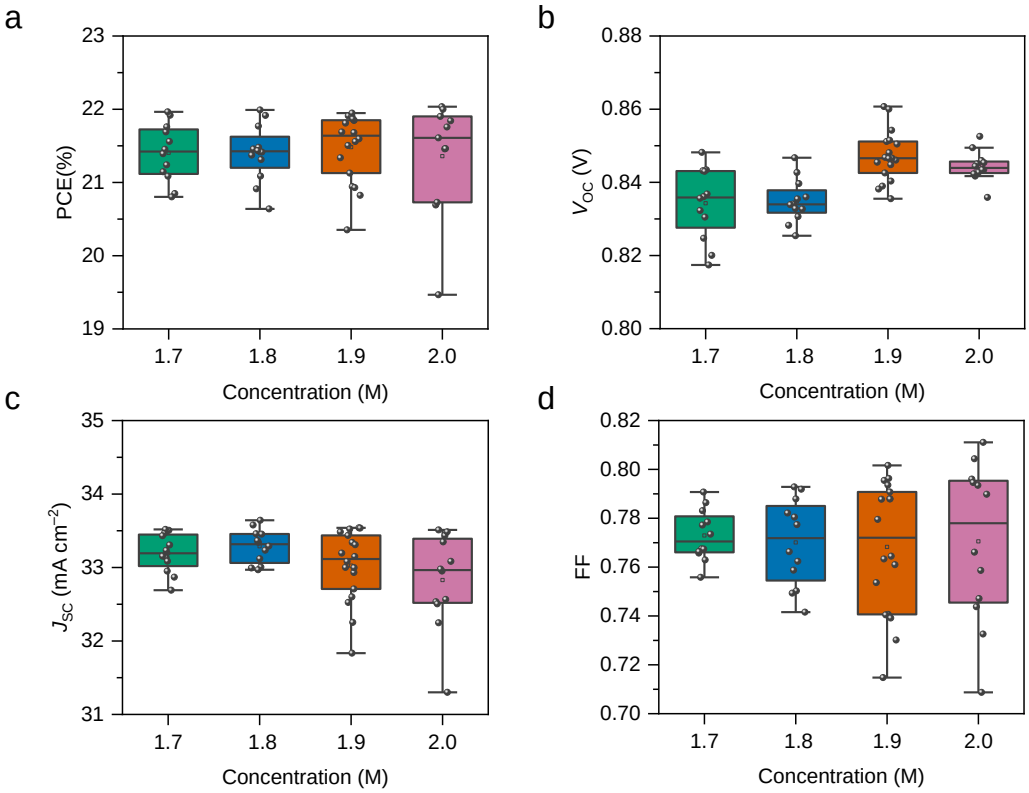

Fig. S37. Statistical distribution of the cell parameters for $EDAI_2$/GlyHCl-treated perovskite devices fabricated with different concentrations of the precursor solution.

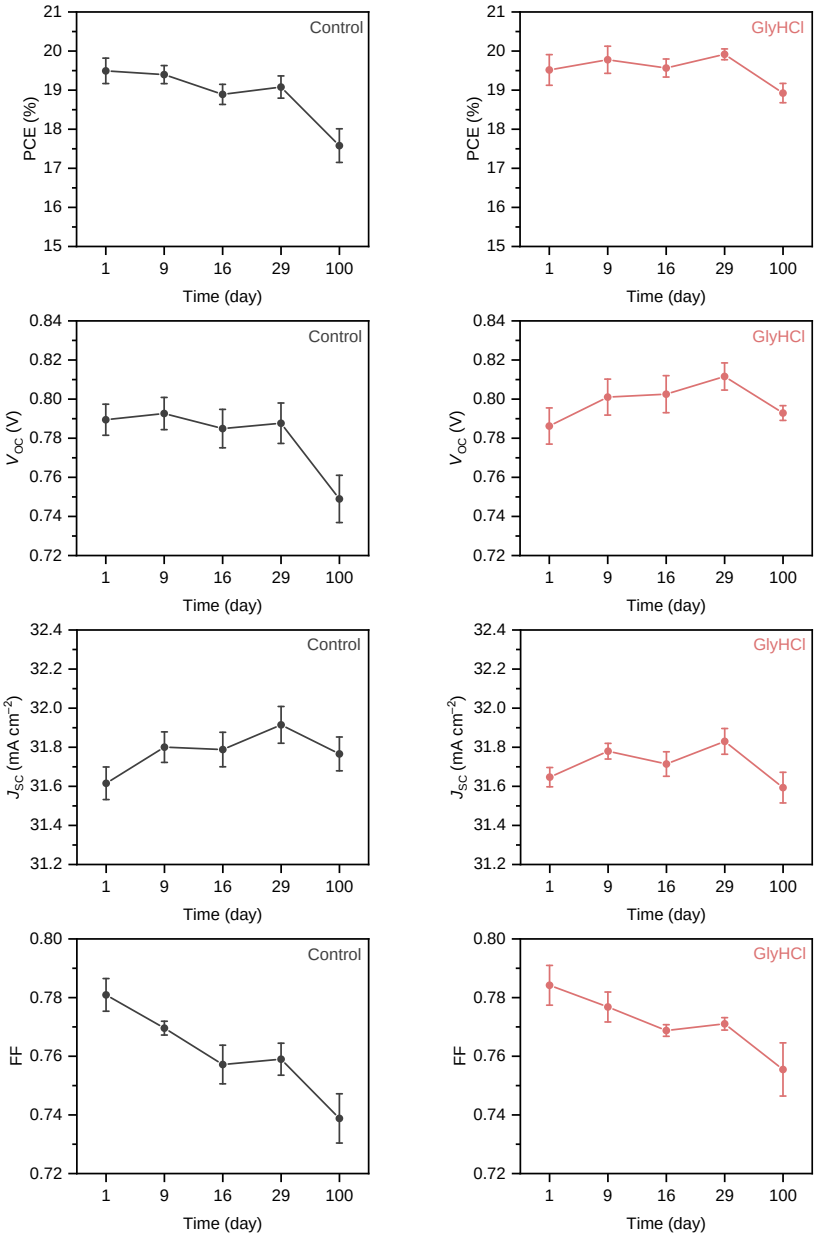

Fig. S38. Shelf-stability of the control and GlyHCl-treated devices stored in the dark in a N_2-filled glovebox. The device parameters are calculated from the average measurements obtained from six cells of each type. After 100 days (2400 h) dark storage in the glovebox, the control device and device treated with GlyHCl additive retained 89% and 97% of their initial efficiencies, respectively.

Impedance characterization

The complex impedance data provides an accurate and detailed picture of the equivalent circuit resistances[8,9]. Representative complex impedance scans for solar cell devices fabricated with the control, $EDAI_2$-treated, and $EDAI_2$/GlyHCl-treated perovskite layers are shown in Fig S39a. The series resistance is minimal, while the parallel resistance, indicated by the diameter of the main semicircular feature, increases from 290 Ω cm^2 for the control film, to 445 Ω cm^2 for the $EDAI_2$-treated and 495 Ω cm^2 for the $EDAI_2$/GlyHCl-treated film. Under the measurement conditions, the parallel resistance (r_p) can be interpreted as the shunt resistance of the perovskite layer, and the higher values of the $EDAI_2$-treated and $EDAI_2$/GlyHCl-treated layers reflect the lower leakage current anticipated from the observed improvement in crystallinity and lower trap densities indicated by the SCLC measurements. The parallel resistance for the three devices values measured over a range of applied bias voltages are compiled in Fig. S39b. The overall trends observed in Fig. S39a are reproduced at all bias voltages below 0.3 V, while as the forward bias increases the resistance values decrease as the recombination currents increase.

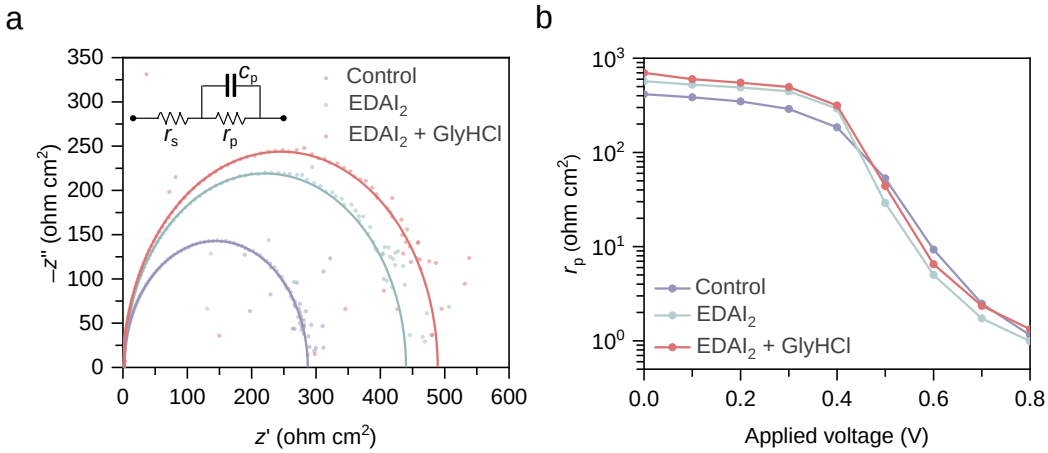

Fig. S39. a, Complex impedance of PSCs scanned over 20 Hz – 20 MHz, recorded at 0.3 V bias under AM 1.5G illumination. **b,** Variations of parallel resistance in log scale as a function of applied voltage.

PLQY characterization

We fabricated perovskite films on PEDOT:PSS to evaluate the nonradiative recombination in our system via PLQY measurement. On PEDOT:PSS, the PLQY of the $EDAI_2$/GlyHCl-treated perovskite film is 2.1% (Fig. S40), considerably higher than that of the control film (~0.001%), verifying that the nonradiative recombination pathways in the $EDAI_2$/GlyHCl-treated films are largely suppressed.

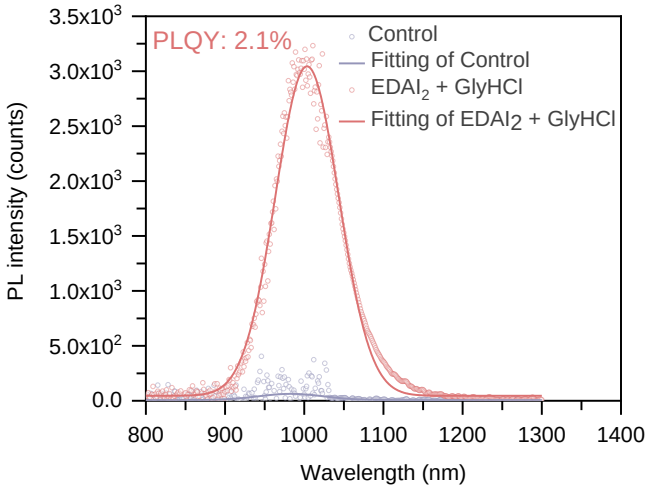

Fig. S40. PLQY spectra of the control and $EDAI_2$/GlyHCl-treated perovskite films excited at 650 nm.

REFERENCES AND NOTES:

1 Tan, S. *et al.* Surface reconstruction of halide perovskites during post-treatment. *J. Am. Chem. Soc.* **143**, 6781–6786 (2021).

2 Shahbazi, S., Li, M.-Y., Fathi, A. & Diau, E. W.-G. Realizing a cosolvent system for stable tin-based perovskite solar cells using a two-step deposition approach. *ACS Energy Lett.* **5**, 2508–2511 (2020).

3 Yamada, Y., Nakamura, T., Endo, M., Wakamiya, A. & Kanemitsu, Y. Photocarrier recombination dynamics in perovskite $CH_3NH_3PbI_3$ for solar cell applications. *J. Am. Chem. Soc.* **136**, 11610–11613 (2014).

4 Yang, D. *et al.* Surface optimization to eliminate hysteresis for record efficiency planar perovskite solar cells. *Energy Environ. Sci.* **9**, 3071–3078 (2016).

5 Zhang, Y. *et al.* Dynamical transformation of two-dimensional perovskites with alternating cations in the interlayer space for high-performance photovoltaics. *J. Am. Chem. Soc.* **141**, 2684–2694 (2019).

6 Dong, Q. *et al.* Electron-hole diffusion lengths >175 μm in solution-grown $CH_3NH_3PbI_3$ single crystals. *Science* **347**, 967 (2015).

7 Shockley, W. & Queisser, H. J. Detailed balance limit of efficiency of p–n junction solar cells. *J. Appl. Phys.* **32**, 510–519 (1961).

8 Zarazúa, I. *et al.* Operating mechanisms of mesoscopic perovskite solar cells through impedance spectroscopy and *J–V* modeling. *J. Phys. Chem. Lett.* **8**, 6073–6079 (2017).

9 Zarazua, I. *et al.* Surface recombination and collection efficiency in perovskite solar cells from impedance analysis. *J. Phys. Chem. Lett.* **7**, 5105–5113 (2016).